

1 **Molecular architecture of 40S initiation complexes on the Hepatitis C virus**
2 **IRES: from ribosomal attachment to eIF5B-mediated reorientation of initiator**
3 **tRNA**

4 **Author List and Affiliations**

5 Zuben P. Brown¹, Irina S. Abaeva², Swastik De¹, Christopher U.T. Hellen², Tatyana V. Pestova^{*2},
6 and Joachim Frank^{*1,3}.

7 ¹Department of Biochemistry and Molecular Biophysics, Columbia University, New York, NY,
8 USA

9 ²Department of Cell Biology, SUNY Downstate Health Sciences University, Brooklyn, NY, USA

10 ³Department of Biological Sciences, Columbia University, New York, NY, USA

11 *Authors for correspondence (Tatyana.Pestova@downstate.edu; jf2192@cumc.columbia.edu)

12 **Lead Contact:** Joachim Frank^{*1,3}

13

14

15

16

17

18 **SUMMARY**

19
20 Hepatitis C virus mRNA contains an internal ribosome entry site (IRES) that mediates end-independent
21 translation initiation, requiring a subset of eukaryotic initiation factors (eIFs). Direct binding of the IRES
22 to the 40S subunit places the initiation codon into the P site, where it base-pairs with eIF2-bound Met-
23 tRNA_i^{Met} forming a 48S initiation complex. Then, eIF5 and eIF5B mediate subunit joining. Initiation can
24 also proceed without eIF2, in which case Met-tRNA_i^{Met} is recruited directly by eIF5B. Here, we present
25 cryo-EM structures of IRES initiation complexes at resolutions up to 3.5 Å that cover all major stages from
26 initial ribosomal association, through eIF2-containing 48S initiation complexes, to eIF5B-containing
27 complexes immediately prior to subunit joining. These structures provide insights into the dynamic network
28 of 40S/IRES contacts, highlight the role for IRES domain II, and reveal conformational changes that occur
29 during the transition from eIF2- to eIF5B-containing 48S complexes that prepare them for subunit joining.

30

31 **Keywords**

32 hepatitis C virus IRES, ribosome, eIF2, eIF5B, translation initiation, cryo-EM

33 INTRODUCTION

34 The canonical initiation process begins with formation of the 43S preinitiation complex
35 (PIC) comprising the 40S ribosomal subunit, the eIF2•GTP/Met-tRNA_i^{Met} ternary complex (eIF2-
36 TC), eIF1, eIF1A and eIF3 (Jackson et al., 2010). The 43S PIC attaches to the capped 5'-terminal
37 region of mRNA and then scans to the initiation codon in a favorable nucleotide context
38 (containing A/G and G at the -3 and +4 positions relative to the AUG, respectively) where it stops
39 and forms the 48S initiation complex (IC) with established codon-anticodon base-pairing.
40 Attachment is mediated by eIFs 4A, 4B and eIF4F, which cooperatively unwind the cap-proximal
41 region allowing attachment and also assist 43S PIC scanning. eIF1, in cooperation with eIF1A,
42 induces an 'open' scanning-competent conformation of the 43S PIC and monitors the fidelity of
43 initiation codon selection (Pestova et al., 1998a; Pestova and Kolupaeva, 2002; Passmore et al.,
44 2007; Hussain et al., 2014). Establishment of codon-anticodon base-pairing in the 48S IC leads to
45 dissociation of eIF1 and eIF5-induced hydrolysis of eIF2-bound GTP, and thereby switches the
46 40S subunit to the 'closed' conformation (Unbehaun et al., 2004; Maag et al., 2005). After that,
47 eIF5B, in its GTP-bound form, displaces residual eIF2•GDP (Pisarev et al., 2006) and promotes
48 joining of the 60S subunit (Pestova et al., 2000). Interaction of eIF5B with eIF1A enhances
49 eIF5B's subunit joining activity and the hydrolysis of eIF5B-bound GTP, leading to coupled
50 release of eIF5B•GDP and eIF1A from the assembled 80S ribosome (Marintchev et al., 2003;
51 Acker et al., 2006; Nag et al., 2016).

52 A number of viral mRNAs contain internal ribosomal entry sites (IRESs), structured RNA
53 regions that mediate cap-independent initiation of translation using a subset of the eIFs that are
54 required by canonical initiation. All IRES-mediated initiation mechanisms are based on non-
55 canonical interactions of IRESs with canonical components of the translation apparatus (Jackson
56 et al, 2010). The ~300nt-long hepatitis C virus (HCV) IRES is located in the 5'-terminal region of
57 the viral genome and epitomizes a class of related RNA elements. HCV-like IRESs occur in the
58 genomes of pestiviruses (e.g., classical swine fever virus (CSFV)), some pegiviruses and numerous
59 members of *Picornaviridae* (Arhab et al., 2020). The HCV IRES comprises three domains (II–
60 IV), with domain III divided into several subdomains (Figure 1A). Ribosomal recruitment of HCV
61 and HCV-like IRESs occurs by direct binding of the IRES to the 40S subunit and does not involve
62 scanning, group 4 eIFs or eIF1 (Pestova et al., 1998b). Domain III binds at the back of the 40S
63 subunit, whereas the long, bent domain II loops out and reaches into the E site. The sites of

64 interaction with the 40S subunit include domains IIIa and IIIc (which bind to eS1, eS26 and eS27),
65 the apex of domain IIId (which base-pairs to expansion segment (ES) 7 of 18S rRNA), domain
66 IIIe (which interacts with helix (h) 26 of 18S rRNA), and the apex of domain II, which interacts
67 with uS7 and eS25 in the head and uS11 on the platform of the 40S subunit, intercalating into the
68 mRNA binding channel and causing tilting of the head and forcing the 40S subunit to adopt the
69 open conformation (Kolupaeva et al., 2000; Kieft et al., 2001; Malygin et al., 2013a; 2013b;
70 Hashem et al., 2013; Angulo et al., 2016; Matsuda and Mauro, 2014; Quade et al., 2015;
71 Yamamoto et al., 2015; Yokoyama et al., 2019).

72 Although domain II does not contribute to the affinity of the HCV IRES to the 40S subunit
73 (e.g. Kieft et al., 2001; Spahn et al., 2001), the open conformation of the 40S subunit promoted by
74 domain II facilitates loading of the region containing the initiation codon into the mRNA binding
75 channel, accounting for the stimulatory role of domain II during initiation on HCV-like IRESs
76 (Honda et al., 1996; Reynolds et al., 1996; Filbin and Kieft, 2011; Odreman-Macchioli et al.,
77 2001). Upon binding to the 40S subunit, domain IV of the HCV IRES unfolds, and the initiation
78 codon is placed in the immediate vicinity of the P site, where it base-pairs with the anticodon of
79 Met-tRNA_i^{Met} as a part of the eIF2-TC, leading to formation of the 48S IC (Pestova et al., 1998b).
80 After that, eIF5 and eIF5B mediate the subunit joining step to complete formation of the
81 elongation-competent 80S ribosome (Locke et al., 2007; Pestova et al., 2008; Terenin et al., 2008).
82 Notably, in 80S complexes assembled on the HCV IRES, the P-site Met-tRNA_i^{Met} and eIF5B•GTP,
83 which correspond to the last stage in the initiation process prior to formation of an elongation-
84 competent ribosome, the tilt of the 40S subunit is reversed, and the apex of domain II is released
85 from its position on the head of the 40S subunit (Yamamoto et al., 2014). Remarkably, when levels
86 of active eIF2 are reduced due to stress-induced phosphorylation, Met-tRNA_i^{Met} can be recruited
87 by eIF5B instead to the IRES/40S complexes (Pestova et al., 2008; Terenin et al., 2008). In both
88 eIF2- and eIF5B-mediated pathways, eIF1A enhances 48S complex formation (de Breyne et al.,
89 2008; Jaafar et al., 2016), whereas eIF1 inhibits the process and even induces dissociation of pre-
90 assembled 48S ICs, but this inhibition can be alleviated by deletion of domain II (Pestova et al.,
91 2008).

92 In addition to 40S subunits, HCV and related IRESs also bind to eIF3 via their apical IIIa
93 and IIIb domains (Pestova et al., 1998b; Sizova et al., 1998; Ji et al., 2004; Hashem et al., 2013).
94 Strikingly, in 40S/IRES/eIF3 complexes, HCV-like IRESs displace eIF3 from its ribosomal

95 position (Hashem et al., 2013), usurping eIF3's key ribosomal contacts involving eS1, eS26 and
96 eS27 (des Georges et al., 2015). Moreover, the ribosome-binding surface of eIF3 is now involved
97 in interaction with the IRES (Hashem et al., 2013). In *in vitro* reconstituted initiation reactions,
98 eIF3 only modestly enhances 48S complex formation on HCV-like IRESs (Pestova et al., 1998b;
99 Hashem et al., 2013), which led to the suggestion that *in vivo*, the role of the eIF3/IRES interaction
100 is likely to relieve the competition between the IRES and eIF3 for a common ribosomal binding
101 site, and to reduce formation of 43S PICs, thereby favoring translation of viral mRNAs (Hashem
102 et al., 2013).

103 Cryo-EM studies have been indispensable in providing insights into the architecture and
104 interactions of HCV and HCV-like IRES ribosomal complexes, as well as the mechanism of the
105 IRES function, initially through low-resolution 40S/HCV IRES and 80S/HCV IRES structures
106 (Spahn et al. 2001; Boehringer et al, 2005) and continuing with sub-nanometer resolution
107 structures of 40S/eIF3/CSFV IRES and 80S/Met-tRNA_i^{Met}/eIF5B•GMPPNP/HCV IRES
108 functional complexes (Hashem et al., 2013; Yamamoto et al., 2014), and the more recent near-
109 atomic resolution reconstructions of 80S•HCV IRES complexes (Yamamoto et al., 2015; Quade
110 et al., 2015; Yokoyama et al., 2019). However, despite these advances, the structures of 48S ICs
111 assembled on the HCV IRES, as well as the transitions between different states in the initiation
112 pathways and accompanying conformational changes have remained unknown. To fill these gaps,
113 we present cryo-EM structures of HCV IRES ribosomal complexes up to 3.5 Å resolution that
114 cover all major stages of IRES-mediated initiation pathways from IRES binding to the 40S subunit
115 through eIF2-containing 48S ICs to the final eIF5B-containing 48S ICs immediately prior to the
116 joining of the 60S subunit. Individually, these structures also provide detailed insights into the
117 dynamic network of contacts between the IRES and the 40S subunit, highlight the role for IRES
118 domain II, and importantly, include the first structure of eIF5B bound to the 40S subunit, prior to
119 subunit joining.

120

121

122

123

124

125

126 **RESULTS AND DISCUSSION**

127

128 ***Overview of cryo-EM analysis of initiation complexes assembled on the wt and the ΔdII HCV***
129 ***IRES with eIF2 or eIF5B***

130 To capture discrete states within either the eIF2- or eIF5B-containing IRES-mediated
131 initiation pathways and to visualize the role of IRES domain II in these processes, initiation
132 complexes were assembled *in vitro* by incubating the *wt* or the ΔdII mutant IRES (Figure 1A) with
133 individual purified translation components. To follow the eIF2-mediated pathway, reaction
134 mixtures were prepared containing the *wt* or the ΔdII IRES, 40S ribosomal subunits, eIF2, eIF3,
135 eIF1A and Met-tRNA_i^{Met}, and to follow the eIF5B-mediated pathway, eIF2 was replaced by eIF5B,
136 thus yielding four discrete sample types (Table S1). Cryo-EM grids of each complex were imaged
137 at 300 kV producing high-contrast micrographs with easily identifiable 40S ribosomal particles
138 (Figure S1A-E; Table S2). The images were processed using maximum-likelihood classification
139 techniques implemented in Relion 3.1 (Scheres, 2012; 2016; Zivanov et al., 2018; 2019) yielding
140 18 structures containing different sets of components at resolutions as high as 3.5 Å (Figure S2;
141 Table S3). Although some flexible regions had a poor local resolution (e.g., eS12 in the 40S head
142 or IRES domain IIIb), most of the ribosome, all IRES-ribosome contacts, and all initiation factors
143 present had resolutions, between 3-7 Å (Figures S2 and S3), that allowed modeling of all these
144 components. None of the structures obtained contained eIF3. During initiation on HCV-like
145 IRESs, eIF3 interacts with the apical region of IRES domain III rather than with the 40S subunit
146 (Hashem et al., 2013). This interaction is sensitive to the process of grid preparation and is more
147 stable when grids have thicker ice so that imaging complexes that contain eIF3 requires the
148 intentional selection of regions with sufficiently thick ice (e.g., Hashem et al., 2013; Neupane et
149 al., 2020); however, our study aimed to determine the details of ribosomal interactions with the
150 IRES, initiation factors and Met-tRNA_i^{Met} at high resolution, which relies on imaging in regions
151 with thinner ice. Importantly, however, the absence of eIF3 does not affect data interpretation
152 because all studied complexes can be assembled efficiently without eIF3 (Pestova et al., 1998b;
153 2008).

154 The structures obtained comprise the 40S/IRES_{ΔdII} binary complex in various
155 conformational states (structures 1_{ΔdII}-9_{ΔdII}); the 40S/IRES_{wt} binary complex in a single
156 conformational state (structure 10_{wt}); the 40S/eIF1A/IRES_{wt} ternary complex (structure 11_{wt}); 48S

157 ICs containing eIF2, Met-tRNA_i^{Met}, eIF1A and the *wt* or the Δ dII IRES (structures 12_{wt} and 12 _{Δ dII});
158 48S complexes containing the *wt* or the Δ dII IRES base-paired with the P-site Met-tRNA_i^{Met} but
159 lacking eIF2 and thus mimicking the stage after eIF2 dissociation following hydrolysis of GTP
160 (structures 13_{wt} and 13 _{Δ dII}); the pre-48S IC containing eIF5B, eIF1A, the *wt* IRES and P-site Met-
161 tRNA_i^{Met} that is not base-paired with the initiation codon (structure 14_{wt}); and 48S ICs containing
162 eIF5B, eIF1A, Met-tRNA_i^{Met} and the *wt* or the Δ dII IRES (structures 15_{wt} and 15 _{Δ dII}) (Figure 1B).

163 Thus, the structures obtained cover the entire initiation pathway, starting with initial
164 binding of the IRES to the 40S subunit and finishing with the eIF5B-containing 48S complex prior
165 to subunit joining, and also provide details of the dynamic interactions between the IRES and the
166 40S subunit (Figures 1C and S4; Table S4).

167

168 ***Stepwise binding of the IRES to the 40S subunit***

169 Binding of the IRES to the 40S subunit involves multiple contacts formed by several IRES
170 domains (IIIa, IIIc, IIId, IIIe, S2) and ribosomal proteins eS1, eS27, eS28 as well as h26 in ES7 of
171 18S rRNA (e.g., Quade et al., 2015; Yamamoto et al., 2015). Deletion or mutation of these domains
172 impairs binding of the IRES to the 40S subunit to different extents, reflecting their cumulative
173 importance for IRES function (Kieft et al., 2001). Strikingly, classification of ribosomal complexes
174 formed on the Δ dII IRES identified a small proportion of 40S/IRES binary complexes that showed
175 conformational differences in the individual positions of IRES domains IIIa/IIIc/IIId/IIIe/IIIif
176 (structures 1 _{Δ dII}-6 _{Δ dII}) compared to other complexes, in all of which these domains had similar
177 positions (structures 7 _{Δ dII}-15_{wt/ Δ dII}) (Figure 1B). The local resolution of the IRES contacts with the
178 40S subunit in these maps was sufficient for model building of all components (Figures S2 and
179 S3) and allowed detailed examination of the relative motion of the Δ dII IRES as it transitioned
180 from a minimally associated state (structure 1 _{Δ dII}) to the canonically bound conformation in which
181 domains IIIa, IIIc, IIId, and IIIe contact eS1, eS27 and h26 (structure 6 _{Δ dII} and structures 7 _{Δ dII}-
182 15_{wt/ Δ dII}).

183 By ordering these structures based on the number of IRES-40S subunit contacts and
184 displacement from the canonically-bound IRES position we produced a putative sequence of
185 binding events between the Δ dII IRES and the 40S subunit (Figure 2A; Table S4). Comparison
186 between the least- and the most- bound states (structures 1 _{Δ dII} and 6 _{Δ dII}) shows that the IRES
187 domains undergo displacement of varying extents during IRES binding (Figure 2B). Across all

188 structures, the most uniform regions of the IRES are the linked domains IIIa and IIIc (Figures 2A-
189 B), which contact eS27 via nt. 163 and 233 as reported (Quade et al., 2015; Yamamoto et al.,
190 2015). Given that these domains undergo minimal structural change regardless of the conformation
191 of the rest of the IRES, the observed impairment of IRES activity by nucleotide substitutions (e.g.,
192 Tang et al., 1999) suggests that these interactions are critical for correct IRES function. Other IRES
193 domains, however, are more dynamic. Thus, to transition from the least- to the most-bound states
194 requires translation of domain IIId by 10.6 Å toward the intersubunit face and domains
195 hIII₁/IIIe/III_f by 23.3 Å toward the mRNA exit channel, whereas domains IIIa/IIIc only move by
196 5.9 Å (Figure 2B).

197 The fully bound IRES forms Watson-Crick base pairs between ES7 nt U₁₁₁₄₋₁₁₁₈ and IRES
198 domains IIId (GGG₂₆₆₋₂₆₈), IIIe (A₂₉₆), and hIII₁ (A₁₃₆) as well as a stacking interaction between
199 domain IIIe (G₂₉₅) and U₁₁₁₅ of ES7 (Quade et al., 2015; Yamamoto et al., 2015). This network of
200 interactions also occurred in the later-stage complexes (structures 6_{ΔdII} and 7_{ΔdII-15_{WT/ΔdI}}) but they
201 were not present during early-stage association of the IRES with the 40S subunit (structure 1_{ΔdII})
202 (Figure 2C; summarized in Figure S4 and Table S4). Initially, the only contact between the IRES
203 and ES7 is a transient and previously undescribed stacking pair between G₂₉₆ in domain IIIe and
204 U₁₁₁₅ of 18S rRNA. Structure 1_{ΔdII} also shows another transient, previously undescribed hydrogen
205 bond between U₂₆₅ in domain IIId and Lys199 in eS1, a residue that instead interacts with IIIe in
206 the fully bound IRES (Quade et al., 2015; Yamamoto et al., 2015). These two contacts along with
207 the domain IIIa/IIIc interactions with eS27 are the only bonds between the IRES and the 40S
208 subunit in this complex (Table S4). In structure 2_{ΔdII}, domain IIId begins to be repositioned, moving
209 by 4.4 Å relative to structure 1_{ΔdII}, and the transient domain IIIe-U₁₁₁₅ contacts are lost. Although
210 the full complement of interactions with ES7 is not present, the Watson-Crick base-pairs between
211 domain IIId (GG₂₆₆₋₂₆₇) and CC₁₁₁₇₋₁₁₁₈ and stacking interactions of G₂₉₅ and A₂₉₆ in domain IIIe
212 with ES7 have formed. These Watson-Crick base pairs and the G₂₉₅ stacking interaction are
213 maintained in all subsequent (structures 2_{ΔdII-6_{ΔdII}}) and fully bound complexes (structures 7_{ΔdII-15_{WT/ΔdI}}),
214 but the A₂₉₆ stacking interaction with U₁₁₁₅ is only present for this and the following
215 complex (structures 2_{ΔdII} and 3_{ΔdII}). Another interaction that first appears in structure 2_{ΔdII} is the eS27
216 Glu75 hydrogen bond with domain IIId nts. 266-267. It is maintained in all subsequent structures
217 except those that have domain II inserted into the E site of the 40S subunit (structures 10_{WT}, 11_{WT}
218 and 14_{WT}; Table S4). In the following complex (structure 3_{ΔdII}), domain IIId is located closer to the

219 platform of the 40S subunit, moving by 2.8 Å; the S1/S2/hIII₁/IIIe/III_f region moves by 5.0 Å,
220 whereas the position of the stable domain IIIa/IIIc changes by only 1.5 Å. This repositioning breaks
221 none of the contacts formed in structure 2_{ΔdII} and allows the formation of a new base-pair between
222 G₂₆₈ in domain IIId and C₁₁₁₆ in ES7. The IRES domains continue to move closer to their canonical
223 bound positions in structure 4_{ΔdII}, which lacks the transient A₂₉₆/U₁₁₁₅ interaction but maintains all
224 other ribosomal contacts (Table S4). In structures 5_{ΔdII} and 6_{ΔdII}, the final canonical interactions of
225 hIII₁ (A₁₃₆) and domain IIIe (A₂₉₆) with ES7 are present. The contact between A₁₃₆ and U₁₁₁₅ is
226 enabled because the base pairing between domain IIIe U₂₉₇ and A₂₈₈ in hIII₁ that induces the
227 flipping-out of A₁₃₆ exists in all structures (1_{ΔdII}-15_{wt/ΔdII}) (Easton et al., 2009). Structures 5_{ΔdII} and
228 6_{ΔdII} are also the first complexes in which the IRES is in a position to form a hydrogen bond between
229 Asn147 in eS1 and the phosphate backbone of GG₃₀₀₋₃₀₁, an interaction that is maintained
230 throughout all subsequent complexes (Table S4).

231 Taken together, this series of structures (1_{ΔdII}-6_{ΔdII}) indicates a likely sequence of binding
232 events between the 40S subunit and the IRES from initial encounter to the canonically-bound
233 conformation in which domain IIIa/IIIc, the first element of the IRES to bind to the 40S subunit,
234 acts as a pivot to dock domain IIId onto ES7. These structures may represent transient states in
235 binding of both the ΔdII and *wt* IRES, which we were able to capture in the former case because
236 the altered kinetic landscape of the initiation pathway in the absence of domain II allowed them to
237 accumulate and be observed.

238 An important corollary of IRES binding is the conformational changes that occur in the
239 40S subunit. Whereas complexes with an incompletely accommodated IRES (structures 1_{ΔdII}-5_{ΔdII})
240 contain 40S subunits in the analogous closed conformation, the ribosomal structures with the full
241 complement of IRES/40S contacts (structure 6_{ΔdII}-9_{ΔdII}) show a striking difference between the
242 position of the head, from the closed conformation in structure 6_{ΔdII} (matching the head position in
243 structures 1_{ΔdII}-5_{ΔdII}) to the fully open state in structure 9_{ΔdII} (Figure 2D-E). Although structures 7_{ΔdII}-
244 9_{ΔdII} have a canonically bound IRES with domain III contacting eS1, eS27 and ES7 as in structure
245 6_{ΔdII}, they show large-scale conformational changes to the head as the 40S subunit transitions from
246 semi-closed (structure 7_{ΔdII}) to fully open (structure 9_{ΔdII}) states. Thus, structure 7_{ΔdII} opens by 3.9°,
247 structure 8_{ΔdII} by 8.1°, and structure 9_{ΔdII} by 10.0° compared to the conformation of the 18S rRNA
248 in structures 1_{ΔdII}-6_{ΔdII}. These global changes to the position of the 40S head are reflected in changes
249 in the P site as the distance between U₁₂₄₈ and C₁₇₀₁ increases from 7.3 Å, to 9.9 Å and finally to

250 11 Å in structures $7_{\Delta\text{dII}}$, $8_{\Delta\text{dII}}$ and $9_{\Delta\text{dII}}$, respectively. Thus, this series of structures shows that even
251 in the absence of domain II, establishment of the full complement of IRES/40S contacts results in
252 the transition of the 40S subunit from the closed to the open state, which is required for
253 accommodation of the initiation codon and surrounding regions in the mRNA-binding channel.

254

255 ***Accommodation of the IRES in the mRNA-binding channel***

256 In contrast to 40S/IRES binary complexes assembled on the ΔdII IRES, which showed
257 remarkable differences in the position of the 40S subunit head, binary complexes assembled on
258 the *wt* IRES yielded a uniform structure that was refined to 3.8 Å resolution from 119,320 particles
259 (structure 10_{wt}) (Figure 1B). Both the conformation of the 40S subunit and the structure of IRES
260 domains IIIa-f in structure 10_{wt} are identical to those in the open state of the 40S/IRES $_{\Delta\text{dII}}$ binary
261 complex (structure $9_{\Delta\text{dII}}$) (Figures 3A-B). There is, however, additional density that corresponds
262 to IRES domain II inserted into the 40S subunit E site, in a conformation that was observed in
263 purified IRES/80S complexes (Quade et al., 2015; Yamamoto et al., 2015). Superposition of
264 structure 10_{wt} and a closed-state 40S subunit shows that in the latter, steric clashes between uS7
265 and domain II would prevent insertion of this domain into the E site. Thus, domain II locks the
266 40S subunit into an open state, which is not similarly imposed in the case of the ΔdII IRES.

267 For the *wt* IRES, we also obtained the structure of the 40S•IRES•eIF1A ternary complex
268 that was refined to 3.8 Å resolution from 204,320 particles (structure 11_{wt} , Figure 1B). The
269 conformation of the 40S subunit and the position of the IRES in it were identical to those in the
270 40S/IRES $_{\text{wt}}$ binary complex (structure 10_{wt}) (Figures 3A-B). The complex clearly showed density
271 for eIF1A located between 18S rRNA helix (h) 44 and the ribosomal proteins eS30 and uS12,
272 allowing us to model the OB domain and the C-terminal subdomain of eIF1A (residues 22-122).
273 Although structure 11_{wt} lacks tRNA and the 40S subunit is in the open state, the position of eIF1A
274 on the ribosome as well as its overall conformation are identical to those in the structures of eIF2-
275 containing 48S complexes (Brito Querido et al., 2020; Simonetti et al., 2020).

276 As expected, binary complexes assembled on the ΔdII IRES and containing the 40S subunit
277 in the closed conformation ($1_{\Delta\text{dII}}\text{-}6_{\Delta\text{dII}}$) do not have mRNA in the mRNA-binding channel.
278 However, although structures $9_{\Delta\text{dII}}$, 10_{wt} and 11_{wt} all have 40S subunits in the identical open
279 conformation that is required for loading of mRNA into the channel, they differ strongly in the
280 degree of ribosomal accommodation of the initiation codon and surrounding regions (Figure 3C).

281 In the 40S/IRES_{ΔdII} binary complex (structure 9_{ΔdII}), clear mRNA density was seen only in the exit
282 portion of the channel up to the -8 position of mRNA (HCV nt 334), after which the mRNA became
283 disordered (Figure 3D). In contrast, in the *wt* 40S/IRES binary complex (structure 10_{wt}), mRNA
284 nucleotides could be identified at the exit channel through the E site where it is stabilized by
285 domain II, to AU₃₄₂₋₃ located in the P site (Figure 3E). The (+3) nucleotide linked to U₃₄₃ could
286 not be identified due to disorder in the map. However, there is additional mRNA density in the
287 mRNA channel ~8 Å from the P-site G₃₄₄, but the identity of these nucleotides does not correspond
288 to those that immediately follow the start codon (A₃₄₅ onwards) as this density extends 20 Å out
289 from the mRNA channel beyond the binding site of eIF1A, suggesting that after the P site, the
290 mRNA is looped out (Figure 3E). Thus, the presence of domain II results in insertion of mRNA
291 into the entire channel, but only the additional 9 nucleotides from the exit to the P site (i.e., from
292 G₃₃₅ to U₃₄₃) can be reliably identified. Density corresponding to mRNA is present from the P site
293 and entry channel but is likely a mixture of different registers of mRNA and so the sequence could
294 not be determined (Figure 3E). Strikingly, the presence of eIF1A in ribosomal complexes resulted
295 in accommodation of sequential mRNA along the entire mRNA binding cleft (Figure 3F).
296 Examination of critical P-site nucleotides for all complexes shows that in each case C₁₇₀₁ of 18S
297 rRNA is in a single conformation, except for the binary complex prepared with the *wt* IRES
298 (structure 10_{wt}) where it is present in two states as determined by examination of the Coulomb
299 potential around that nucleotide (Figure 3G). In the conformation of the second state, C₁₇₀₁ contacts
300 the upstream mRNA base U₃₄₃, possibly contributing to stabilizing the mRNA when it has not
301 undergone complete accommodation in the mRNA channel at the P site. The highly conserved
302 C₁₆₉₈ (Prince et al., 1982) contacts downstream mRNA and may act as a sensor to stimulate C₁₇₀₁
303 adopting the second conformation in which it can stabilize the incompletely loaded mRNA (Figure
304 3G).

305 The position of the mRNA in structures 10_{wt} and 11_{wt}, however, does not match its position
306 in 48S complexes with an established codon-anticodon interaction (Brito Querido et al., 2020;
307 Simonetti et al., 2020). Beginning from the (-1) position, the following (+1), and (+2) nucleotides
308 are ~4 Å above their position when tRNA is inserted (Figures 3H-I). However, the raised position
309 of these nucleotides in the complex containing eIF1A nevertheless allows the (+4) adenine base to
310 form the stacking triple with eIF1A Trp70 and 18S rRNA A₁₈₂₅ (Figure 3I), which is a key function

311 of eIF1A (Battiste et al., 2000). These contacts are maintained up to formation of 48S complexes
312 (Simonetti et al., 2020).

313 Taken together, the structures of binary complexes assembled on Δ dII and *wt* IRESSs and
314 the eIF1A-containing complex assembled on the *wt* IRES provide structural rationalization for the
315 roles of domain II and eIF1A in sequentially loading the mRNA channel. Even without domain II,
316 binding of the IRES induces conformational changes in the 40S subunit that are required for
317 accommodation of mRNA in the binding channel. However, accommodation in this case is only
318 partial, and the 40S subunit is not stably present in the open conformation, which is consistent, on
319 one hand, with the ability of Δ dII IRES to function in initiation, but on the other hand, with lower
320 initiation activity than the *wt* IRES (e.g., Reynolds et al., 1996). The presence of domain II results
321 in accommodation of the initiation codon and the upstream region in the mRNA-binding channel,
322 thereby enhancing the efficiency of initiation (Reynolds et al., 1996), whereas addition of eIF1A
323 results in further accommodation of the mRNA in the entire mRNA-binding channel, accounting
324 for its enhancement of initiation on the IRES (Jaafar et al., 2016).

325

326 ***The structure of eIF2-containing 48S complexes assembled on the HCV IRES***

327 The structures of eIF2-containing 48S ICs assembled on the *wt* and Δ dII IRES were refined
328 from 46,904 and 103,813 particles to resolutions of 3.6 and 3.5 Å, respectively (structures 12_{wt}
329 and 12 _{Δ dII}, Figures 1B and S1). Both *wt* and Δ dII IRES 48S ICs form identical complexes with
330 respect to the 40S subunit's closed conformation, the positions of Met-tRNA_i^{Met}, eIF2 and eIF1A,
331 and the established P-site codon-anticodon base pairing (Figures 4A, and S5A-B). The IRES-
332 containing 48S IC is also structurally identical to the canonical 48S complex formed by cap-
333 dependent initiation (e.g., Simonetti et al., 2020) with respect to the global conformation of the
334 40S subunit as well as the placement of Met-tRNA_i^{Met}, eIF2 α , and eIF1A. Thus, the E site-
335 associated eIF2 α contacts the highly conserved uS7/Asp194 directly and interacts with Met-
336 tRNA_i^{Met} via Thr103, Arg67 and His114 (Figure 4B). As with yeast 48S ICs (Hussain et al., 2014),
337 eIF2 α forms hydrogen bonds with the (-3) adenosine via Arg55, a contact that enhances codon
338 selection in the scanning mode of initiation, presumably by stabilizing the arrested 48S IC (Pisarev
339 et al., 2006; Thakur et al., 2020). Contacts between eIF2 α Arg57 and the tRNA acceptor stem loop
340 (ASL) and the 18S rRNA that occur in canonical 48S ICs are also present (Simonetti et al., 2020)
341 (Figure 4B). The position of eIF2 α is identical in *wt* and Δ dII IRES 48S ICs (Figure S5E). The

342 unsharpened map also contained density corresponding to eIF2 γ (Figure S5D) identical to that seen
343 in cap-dependent 48S initiation complexes (Simonetti et al., 2020), but it had a low local resolution
344 at the acceptor end of Met-tRNA_i^{Met} and was not modelled after map sharpening.

345 The position of domain II differs substantially between the 48S IC assembled on the *wt*
346 IRES (structure 12_{wt}) and the corresponding 40S/IRES binary and 40S/eIF1A/IRES ternary
347 complexes (structures 10_{wt} and 11_{wt}). In both the binary and ternary complexes, it is inserted into
348 the E site, a position that is incompatible with the binding of eIF2. Thus, in the 48S IC, domain II
349 is oriented away from the subunit interface, towards the solvent side of the 40S subunit, and shows
350 an attenuation of density so that a model of domain II is not fully enclosed by the map. Focused
351 classification of this region revealed that domain II is flexible and occupies multiple conformations
352 oriented away from the E site (Figure 4C; Figure S5F; Table S5).

353 Compared with the binary or ternary complexes (structures 10_{wt} and 11_{wt}), the head of 48S
354 ICs formed on both *wt* and Δ dII IRESs is in a closed position, having moved by 11.2° relative to
355 the open states (Figure 4D), and is in an even more closed conformation than in closed binary
356 complexes (structures 1 _{Δ dII}-6 _{Δ dII}), in which the position of the head differed from that in structures
357 10_{wt} and 11_{wt} by ~9.0° (Figure 3A).

358 Comparison between the ternary complex (structure 11_{wt}) and the 48S IC (structure
359 12_{wt/ΔdII}) shows the effect that incorporation of tRNA into the P site and rearrangement of 18S
360 rRNA into the closed conformation has on the position of mRNA in the mRNA-binding channel.
361 The raised position of P-site mRNA in the ternary complex (Figure 4E) cannot be maintained as
362 this would cause a clash with the P-site tRNA in the 48S IC (Figure 4F). Thus, upon 40S subunit
363 closure and incorporation of P-site tRNA, the mRNA repositions ~4 Å deeper into the mRNA
364 channel and the A(+4) base flips out to maintain the stacking triple with eIF1A Trp70 and 18S
365 rRNA A₁₈₂₅ that is seen in the ternary complex (Figures 4E-F). The mRNA is also shifted upstream
366 due to the movement of eS28 in the ribosome head (Figure 4G). A network of hydrogen bonds in
367 the ternary complex (structure 11_{wt}) between multiple arginines in eS28 and the mRNA is reformed
368 by the displacement of eS28 in the closed complex (structure 12_{wt/ΔdII}). Arg69 contacts the guanine
369 at (-7) position in the ternary complex, but the shift of the 18S rRNA to the closed position causes
370 this leading contact to be broken and reformed with G(-5). Other contacts are similarly
371 reorganized, and the Arg31 contact with the stacked G₃₃₁-G₃₀₇ pair is lost completely (Figure 4G-
372 H). This reorganization of contacts causes the mRNA to shift by one base pair at the P site and

373 allows contact with the tRNA anticodon arm once tRNA is inserted into the P site. Interestingly,
374 eIF2 α Arg55 contacting the mRNA at A(-3) is in the same position as C₈₃ in IRES domain II in
375 the 40S/eIF1A/IRES ternary complex, which could indicate that this location in the E site is
376 important for stabilizing the mRNA regardless of the conformation of the 40S subunit and
377 differences in position of mRNA at other locations along the mRNA-binding channel (Figure 4I).

378 Interestingly, we also obtained 40S ribosomal complexes containing platform-bound *wt* or
379 Δ dII IRES and P-site Met-tRNA_i^{Met} but lacking all initiation factors (structures 13_{wt} and 13 _{Δ dII})
380 (Figure 1C). These closed complexes, refined from 15,906 and 15,598 particles to 4.6 and 4.4 Å,
381 respectively, clearly showed density for codon-anticodon base pairing (Figure S3G; Table S3). It
382 is unclear whether initiation factors dissociated due to slow eIF5-independent hydrolysis of eIF2-
383 bound GTP (Unbehaun et al., 2004), or through denaturation at the air-water interface and/or due
384 to the shear forces associated with blotting (Glaeser, 2021; d’Imprima et al., 2019). In any case,
385 this complex likely mimics an intermediate state immediately after eIF2 dissociation and prior to
386 the binding of eIF5B.

387

388 ***The structure of eIF5B-containing 48S complexes assembled on the IRES***

389 Classification of eIF5B-containing ribosomal complexes yielded two structures formed on
390 the *wt* IRES (structures 14_{wt} and 15_{wt}) and one structure (15 _{Δ dII}) assembled on the Δ dII IRES
391 (Figures 1B and S1). Structures 14_{wt}, 15_{wt} and 15 _{Δ dII} were refined to 3.8 Å, 3.7 Å and 3.7 Å
392 resolution from 60,578, 133,782 and 61,648 particles, respectively (Figures 5A-B and S6A). All
393 structures contain eIF5B, eIF1A and the P-site Met-tRNA_i^{Met}. However, whereas structures 15_{wt}
394 and 15 _{Δ dII} showed density for the base-paired codon-anticodon and were accordingly classified as
395 48S ICs, the P-site Met-tRNA_i^{Met} was not base-paired with the initiation codon in structure 14_{wt},
396 which was therefore designated as a pre-48S IC (Figure S3G). Similar to eIF2-containing 48S ICs
397 assembled on the *wt* IRES, in eIF5B-containing ICs assembled on the *wt* IRES (structure 15_{wt})
398 domain II is oriented away from the subunit interface, toward the solvent side of the 40S subunit,
399 and shows an attenuation of density that can be resolved by focused classification into multiple
400 states (Figure 1B and S6B; Table S5). In contrast to structures 15_{wt/ Δ dII} that are in an identical
401 closed conformation, the 40S subunit in structure 14_w is in an open conformation with domain II
402 inserted into the E site (Figure S6C). In all structures, eIF1A occupies its usual position over h44

403 and eS30 and uS12, whereas eIF5B resides on the intersubunit face of the 40S subunit as in 80S
404 ribosomal complexes (Yamamoto et al., 2014; Huang and Fernandez, 2020; Wang et al., 2020).

405 The structures show clear density for eIF5B residues 592-1218, corresponding to all major
406 domains. The G domain, and domains II and III form the central domains of eIF5B that connect
407 via domain III and helix 12 to the tRNA acceptor stem binding domain IV. (Figure 5C). This is
408 the first high-resolution structure of mammalian eIF5B and also the first structure of the 40S/eIF5B
409 subunit complex prior to subunit joining. Although we used full-length native eIF5B, extensive
410 3D classification and processing did not reveal any structure corresponding to the N-terminal
411 region, suggesting that the structure in this region is highly disordered, an observation that is
412 supported by the structure of full-length eIF5B from a range of species predicted using AlphaFold
413 (Jumper et al., 2021). Consistent with the requirement of the 60S subunit for induction of eIF5B's
414 GTPase activity (Pestova et al., 2000), all complexes contained eIF5B-bound GTP (Figure S6E).
415 Previous structures of mammalian eIF5B determined at ~9 Å resolution used GMPPNP and
416 showed the GDP-bound conformation of switch 1 (Yamamoto et al., 2014) (Figure S7A). In
417 contrast, all our complexes showed switch 1, switch 2, and the β9-β10 loop in domain II in the
418 GTP-bound conformation (Kuhle and Ficner, 2014). The conformation of this conserved GTP-
419 binding region of mammalian eIF5B is identical to that in fungal eIF5B (Kuhle and Ficner, 2014;
420 Wang et al., 2020) (Figure S7B-D).

421 We identified multiple contacts between eIF5B domains II and III and 18S rRNA h5, h14,
422 and h15, as well as an interaction between eIF5B domain II and uS12 (Table S6; Figure S6D), and
423 noted that the β13-β14 loop in our complexes could interfere with the transition of switch 1 from
424 GTP-bound to GDP-bound conformations (Kuhle and Ficner, 2014) (Figure S6F). On the yeast
425 80S ribosome, the β13-β14 loop of eIF5B contacts A₄₁₅ in 18S rRNA h14 and is positioned away
426 from the path that switch 1 might take as it changes to the GDP-bound conformation (Wang et al.,
427 2020). Although there is no contact between the equivalent nucleotide (A₄₆₄) and β13-β14 in our
428 complexes, h14 is accessible. These observations suggest that the 60S subunit might stimulate the
429 interaction between A₄₁₅ and the β13-β14 loop to reposition this loop away from switch 1 so that
430 a transition from GTP- to GDP-bound conformation. In both pre-48S ICs and 48S ICs, the position
431 of domain IV also allows it to contact eIF1A via interactions between His112 in the helical
432 subdomain of eIF1A (Battiste et al., 2000) and the extreme C-terminal region of eIF5B, as well as
433 between the eIF1A L23 beta-turn (near Gly54) and Arg1186 in domain IV of eIF5B (Figure 5D).

434 These interactions are distinct from the previously reported binding of eIF1A's extreme C-terminal
435 DDIDI sequence to the h12/h13 loop in eIF5B domain IV (Marintchev et al., 2003; Zheng et al.,
436 2014) and of the eIF1A L45 loop to eIF5B domain III (Nag et al., 2016).

437 Comparison of the position of the P-site Met-tRNA_i^{Met} in the eIF2-containing 48S IC
438 (Simonetti et al., 2020) and in the 80S ribosome (Yamamoto et al., 2014; Wang et al., 2020) shows
439 when the large subunit is present, tRNA rotates 14° towards the 40S subunit body and the T-loop
440 moves by ~ 15 Å to allow placement of the acceptor stem into the P site of the 60S subunit. We
441 therefore examined our maps (structures 12_{wt/ΔdII}-15_{wt/ΔdII}) to determine how the orientation of the
442 P-site tRNA differs in 40S ribosomal complexes depending on the presence of eIF2 or eIF5B.
443 Compared to eIF2-containing 48S ICs, in eIF5B-containing complexes, Met-tRNA_i^{Met} rotates by
444 ~14° and moves by 15 Å from the head of the 40S subunit to a position that matches the orientation
445 seen in 80S structures (Wang et al., 2020) (Figure 5C). This repositioning of tRNA was observed
446 for all structures that contained eIF5B, regardless of whether the 40S subunit was in the open (pre-
447 48S IC) or closed (48S IC) conformation (Figure 5C), indicating that eIF5B re-oriens Met-
448 tRNA_i^{Met} on the 40S subunit at the 48S PIC stage prior to subunit joining. Interestingly, although
449 the overall position of eIF5B-Met-tRNA_i^{Met} in eIF5B-containing 48S ICs and in 80S ribosomes is
450 similar, upon binding of a 60S subunit, domain IV of eIF5B undergoes a 33° rotation towards the
451 platform side of the 40S subunit as well as a translation by 6.4 Å parallel to the mRNA channel
452 towards the platform of the 40S subunit, which results in repositioning of the tRNA acceptor stem
453 by 6.4 Å toward the ribosome head (i.e., toward ribosomal protein eS25) without changing the
454 position of the ASL (Figure 5E-F). The repositioning of eIF5B domain IV occurs despite an only
455 minor movement of helix 12 (Figure 5F; Figure S6G). Such repositioning of domain IV and the
456 tRNA acceptor stem upon binding of a 60S subunit would avert steric clashes of domain IV with
457 H84 of 28S rRNA and between uL16 and the tRNA acceptor stem (~A74) (Figure 5F). Similar
458 repositioning of IF2 domain C2 (equivalent to eIF5B domain IV) to avoid analogous steric clashes
459 was observed in bacteria upon joining of 50S subunits to 30S ICs (Hussain et al., 2016).
460 Adjustment of the orientation of initiator tRNA prior to subunit joining is a critical step in
461 initiation, and the mechanism by which it is mediated, by rotation and translation of domain IV of
462 the universally conserved initiation factor IF2/eIF5B, likely appeared early in evolution.

463 Despite the differences in the orientation of the acceptor arm of the P-site tRNA in
464 ribosomal complexes containing eIF2 and eIF5B, as well as differences in the conformation of the

465 40S subunit in eIF2/eIF5B-containing 48S ICs and eIF5B-containing pre-48S ICs, the anticodon
466 loop in all these complexes is identically positioned (Figure 5D). eIF5B- and eIF2-containing 48S
467 ICs assembled on the IRES are also in the same closed conformation (Figures S6C), identical to
468 that in 48S ICs assembled on canonical cap-dependent mRNA (Simonetti et al., 2020). Thus, in
469 eIF5B- and eIF2-containing 48S ICs, 18S rRNA nucleotides C₁₇₀₁ and U₁₂₄₈ are separated by ~3.5
470 Å, and the contacts of the P-gate nucleotides G₁₆₃₉ and A₁₆₄₀ in the 18S rRNA and Arg146 in uS9
471 with the tRNA anticodon arm on the opposite side to the anticodon are also present in both 48S
472 ICs.

473 In contrast, the 40S subunit in the eIF5B-containing pre-48S IC is in the open
474 conformation, in which the separation between C₁₇₀₁ and U₁₂₄₈ is increased to ~11 Å, and there are
475 no contacts between the tRNA and the P gate or uS9 (Figure 5H). As with the 40S/eIF1A/IRES
476 ternary complex (structure 11_{wt}), the open configuration of the ribosome head present in the pre-
477 48S IC creates a network of hydrogen bonds between the mRNA and eS28 (Figure S7E) that causes
478 the mRNA to be shifted by one nucleotide relative to the closed configuration (Figure S3G). This
479 results in the final nucleotide of the start codon (G₃₄₄) being out of place in the P site and not
480 participating in any contacts with the tRNA anticodon. Instead, G₃₄₄ is available to form a stacking
481 triple with eIF1A Trp70 and A₁₈₂₅ of 18S rRNA (Figure 5H). In the closed conformation of 48S
482 ICs, the hydrogen bonds with eS28 have been partially broken (Figure S7F) and so all three
483 nucleotides of the start codon are accommodated in the P site, and the A(+4) nucleotide is available
484 to form a stacking triple with eIF1A Trp70 and A₁₈₂₅ of 18S rRNA (Figure 5F and 5I).

485

486 ***Comparison of eIF5B-containing pre-48S initiation complexes with eIF2-containing scanning***
487 ***43S complexes***

488 In contrast to initiation on the HCV IRES, eIF5B cannot substitute for eIF2 in recruiting
489 Met-tRNA_i^{Met} to the 40S subunit in the canonical scanning mechanism. Canonical initiation also
490 requires eIF1, which binds to the 40S subunit below the mRNA channel at the P site between h24
491 and the region connecting h44 to h45 and, in cooperation with eIF1A, induces the open
492 conformation of the 40S subunit (Passmore et al., 2007; Llácer et al., 2015), thereby promoting
493 ribosomal attachment to mRNA, scanning and initiation codon selection (e.g., Pestova and
494 Kolupaeva, 2002). We therefore compared the conformation of the 40S subunit and the positions
495 of mRNA and Met-tRNA_i^{Met} in eIF5B-containing pre-48S complexes formed on the *wt* IRES

496 (structure 14_{WT}) and in canonical scanning eIF2-containing 43S complexes that also contained eIF1
497 (Brito Querido et al., 2020).

498 Even though the individual mRNA bases could not be identified in the scanning, eIF2-
499 containing 43S complex because the P site nucleotides were heterogenous (Brito Querido et al.,
500 2020), the positions of mRNA in this complex and in the eIF5B-containing pre-48S complex are
501 very similar (Figure 6A). Although codon-anticodon base-pairing is not established in either
502 complex, the anticodon loops of Met-tRNA_i^{Met} in both are poised to contact mRNA and base-pair
503 with an initiation codon, which is in contrast to the P_{OUT} position of tRNA in fully open mRNA-
504 free 43S complexes (Kratzat et al., 2021), in which the anticodon loop is positioned too far away
505 to be able to interact with mRNA if it had bound in the P site (Figure S7G). However, whereas the
506 conformations of the anticodon in the P site in both complexes are similar, in the eIF5B-containing
507 complex, the T-arm and the acceptor stem are shifted toward the body of the 40S subunit by
508 bending of the anticodon loop region (Figure 6B). Consequently, the contacts between the ASL of
509 Met-tRNA_i^{Met} and 18S rRNA nucleotides GA₁₆₃₉₋₄₀ and the N-terminal region of uS9 in the head
510 of the 40S subunit, which are present in all eIF2-containing complexes, including mRNA-free and
511 scanning 43S complexes and 48S ICs (e.g., Hussain et al., 2014; Brito Querido et al., 2020;
512 Simonetti et al., 2020), do not exist in the eIF5B-containing pre-48S ICs and only form after codon-
513 anticodon base-pairing (Figure 6B). Thus, interaction with eIF2 allows tRNA to maintain the
514 contacts with the head of the 40S subunit in all conformations, from fully open to fully closed, and
515 the position of the anticodon loop that allows it to inspect mRNA in the scanning 43S complexes
516 is determined by the rotation of the head that is in the intermediate conformation compared to fully
517 open and fully closed states. In contrast, when interacting with eIF5B, tRNA establishes these
518 contacts only in the closed position of the head, whereas in the open pre-48S ICs tRNA is stabilized
519 by contacts between eIF5B domain IV and the acceptor stem, tRNA anticodon U₃₅ and mRNA
520 A(+1), and a single 18S rRNA nucleotide (C₁₇₀₁) that partially stacks with C₃₃ (instead of the
521 stacking of both U₁₂₄₈/C₁₇₀₁ as in the closed case) (Figure 6B). Thus, whereas some aspects of
522 eIF5B-containing pre-48S complexes are analogous to those of eIF2-containing scanning 43S
523 complexes, the overall orientation, and the specific interactions of tRNA in them differ.

524 In eIF5B pre-48S complexes, the open conformation of the 40S subunit is supported by the
525 insertion of IRES domain II into the E site, whereas in eIF2-containing complexes, the
526 conformation of the 40S subunit is determined by the binding of eIF1. We therefore analyzed

527 whether binding of eIF1 would be compatible with the structure of eIF5B-containing pre-48S ICs.
528 The position of eIF1 placed into such complexes suggests that it would clash with tRNA. Thus,
529 the repositioning of tRNA in eIF5B-containing complexes causes the AAC₃₈₋₄₀ nucleotides of Met-
530 tRNA_i^{Met} to move toward the 40S subunit body by ~3.0 Å, so that the binding of eIF1 as in the
531 43S scanning complex would create a clash between A₃₆ of Met-tRNA_i^{Met} and the β1-β2 loop
532 (Figure 6C). Accommodation of eIF1 would require either reorganization of this loop or
533 displacement of the P-site tRNA. Examination of human (Fletcher et al., 1999) and yeast (Reibarkh
534 et al., 2008) solution NMR structures of eIF1 did not identify any conformations of the β1-β2 loop
535 that would allow a clash with the anticodon stem of tRNA to be avoided in the eIF5B-containing
536 pre-48S and 48S ICs. Moreover, the eIF1 β3-β4 loop would also clash with tRNA nucleotides
537 GU₂₃₋₂₄, and a clash between Phe113 and tRNA nucleotide G₂₅ is also possible (Figure 6C). These
538 observations suggest that even if eIF5B were able to bind Met-tRNA_i^{Met} with high affinity and
539 recruit it to the 40S subunit efficiently, the structure of the resulting complexes would not be
540 compatible with binding of eIF1 and hence, with the scanning mechanism of initiation. On the
541 other hand, the stabilizing interaction of the acceptor arm of Met-tRNA_i^{Met} with domain IV of
542 eIF5B in the closed 48S complexes following dissociation of eIF2•GDP and eIF1 would lock the
543 complex preventing leaky scanning from occurring.

544 The incompatibility of Met-tRNA_i^{Met} and eIF1 on eIF5B-containing pre-48S complexes
545 likely explains why eIF1 disrupts 48S complexes prepared using *wt* but not the ΔdII variant of the
546 HCV-like CSFV IRES (Pestova et al., 2008). HCV domain II has the propensity to insert into the
547 E site (Quade et al., 2015; Yamamoto et al., 2015), locking the ribosome into the open
548 conformation, and the structurally related CSFV domain II likely behaves similarly. As outlined
549 above, the tRNA consequently loses contacts with uS9, with GA₁₆₃₉₋₄₀ as well as with U₁₂₄₈. If
550 eIF1 binds to this complex, then the insertion of its β1-β2 loop into the mRNA channel creates
551 steric hindrance between mRNA and tRNA in the P site, dislodging the tRNA.

552 CONCLUDING REMARKS

553 Here we present the most comprehensive structural overview of the HCV IRES-mediated
554 initiation pathway to date (Figure 7). The IRES initially binds to the 40S subunit through domains
555 IIIa/IIIc and then pivots onto its platform side where it establishes the complete set of contacts
556 (structures 1_{ΔdII}-6_{ΔdII}). Once the canonical set of contacts are made, this induces the head of the
557 ribosome to open (structure 8_{ΔdII}-9_{ΔdII}). Although head opening can occur in the absence of IRES

558 domain II, such complexes are nevertheless characterized by remarkable heterogeneity in the
559 position of the 40S subunit head. In contrast, 40S/IRES binary complexes assembled on the *wt*
560 IRES yield a uniform structure, in which the 40S subunit is in the open conformation, and domain
561 II is inserted into the E site (structure 10_{wt}). Importantly, in the absence of domain II, mRNA
562 density was clearly seen only in the exit portion of the channel up to the -8 position of mRNA
563 (structure 9_{ΔdII}), whereas in the *wt* 40S/IRES binary complex, mRNA nucleotides could be
564 identified at the exit channel through the E site where it is stabilized by domain II, to AU₃₄₂₋₃
565 located in the P site (structure 10_{wt}), and eIF1A induces further accommodation of the mRNA in
566 the entire mRNA-binding channel (structure 11_{wt}). Thus, these complexes provide structural
567 insights into the functions of multiple IRES domains, including IIIa/IIIc in establishing the initial
568 ribosome contacts, IIId in fixing the IRES to the 40S subunit and inducing ribosomal head opening,
569 and II in imposing the open conformation and promoting fixation of mRNA in and upstream of
570 the P site. Our analysis also revealed the role of eIF1A in completing mRNA accommodation.

571 Once the mRNA is loaded, initiation can proceed either along the canonical initiation
572 pathway, in which eIF2 promotes attachment of Met-tRNA_i^{Met} to form the 48S IC (structure
573 12_{wt/ΔdII}) and then dissociates after GTP hydrolysis (likely structure 13_{wt/ΔdII}) followed by binding
574 of eIF5B (structure 15_{wt/ΔdII}), or by a shortcut route, in which Met-tRNA_i^{Met} is loaded directly by
575 eIF5B, first forming open pre-48S ICs without established codon-anticodon interaction (structure
576 14_{wt}) and then locking upon codon-anticodon base-pairing (structure 15_{wt}). The eIF2-containing
577 48S ICs assembled on the IRES are structurally identical to canonical 48S ICs with respect to the
578 conformation of the 40S subunit and the positions of Met-tRNA_i^{Met}, eIF2 and eIF1A. The position
579 of domain II of the IRES in 40S/IRES_{wt} binary complexes is incompatible with binding of eIF2
580 and the closed conformation of the 40S subunit, and consequently, in 48S ICs, domain II is oriented
581 away from the subunit interface, toward the solvent side, occupying multiple conformations
582 oriented away from the E site. In eIF5B-containing pre-48S ICs, the 40S subunit is in the open
583 conformation and domains II is inserted into the E site. Upon codon-anticodon base-pairing in
584 eIF5B-containing 48S ICs, the 40S subunit adopts the closed conformation, and domain II
585 becomes displaced from the E site and is oriented away from the subunit interface like in eIF2-
586 containing 48S ICs. Importantly, compared to eIF2-containing 48S ICs, in eIF5B-containing pre-
587 48S ICs and 48S ICs, Met-tRNA_i^{Met} rotates by ~14° and moves 15 Å from the head of the 40S
588 subunit to a position that matches the orientation in 80S ribosomes. Thus, our data show how

589 eIF5B repositions tRNA already on the 48S complex, thus preparing it for joining with the 60S
590 subunit.

591

592

593

594

595

596

597

598

599

600

601

602

603

604

605

606

607

608

609

610

611

612

613

614

615

616

617

618

619

620

621 **Acknowledgments**

622 This work was supported by NIH R01 GM55440 (to J.F.), R35 GM139453 (to J.F.), R35
623 GM122602 (to T.V.P.), and R01 AI123406 (to C.U.T.H.) Cryo-EM data were collected at the
624 Columbia University Cryo-Electron Microscopy Center.

625 **Author Contributions**

626 Conceptualization, T.V.P., C.U.T.H., and J.F.; Investigation, Z.P.B., and I.A.; Validation Z.P.B.,
627 I.A., and S.D.; Writing – Original Draft, T.V.P. and Z.P.B.; Writing – Review and Editing, Z.P.B.,
628 I.A., S.D., C.U.T.H., T.V.P., and J.F.; Funding Acquisition, C.U.T.H., T.V.P., and J.F.;
629 Supervision, C.U.T.H., T.V.P., and J.F.

630 **Declaration of Interests**

631 Authors declare no competing interests.

632

633

634

635

636

637

638

639

640

641

642

643

644

645

646

647

648

649

650

651

652 **FIGURE LEGENDS**

653

654 **Figure 1. Overview of HCV IRES-mediated initiation complexes.**

655 (A) Secondary structure of the HCV IRES.

656 (B) Segmented maps of labeled IRES ICs, showing the 40S subunit (yellow), IRES (red), eIF1A
657 (blue), Met-tRNA_i^{Met} (magenta), and initiation factors eIF2 or eIF5B (green). Complexes were
658 assembled on the *wt* or Δ dII IRES. Complexes that share identical 40S subunit conformation and
659 factor composition are enclosed by dashed lines.

660 (C) Contacts between the IRES and 40S subunit. Ribosomal proteins (red), 18S rRNA (yellow),
661 and the AUG codon (blue) are marked for the labeled complexes. Complete pathway in Figure S4
662 and Table S4.

663 See also Figures S1-S4 and Tables S1-S4.

664

665 **Figure 2. Initial events during binding of the HCV IRES to the 40S subunit.**

666 (A) IRES models from structures 1 $_{\Delta}$ dII-6 $_{\Delta}$ dII aligned on the 40S subunit. IRES domains and
667 ribosomal proteins eS1 (blue), eS27 (magenta) and 18S rRNA ES7 (yellow) are indicated (inset).

668 (B) Comparison between minimally bound (structure 1 $_{\Delta}$ dII) and fully bound (structure 6 $_{\Delta}$ dII) IRES
669 complexes showing the displacement of labeled IRES domains.

670 (C) Formation of critical contacts between ES7 and the IRES requires reorganization of domains
671 hIII₁, IIIe, and IIId. The arrows indicate displacement of IRES nucleotides A₁₃₆ (hIII₁), G₂₉₅/A₂₉₆
672 (IIIe) and GGG₂₆₆₋₂₆₈ (IIId) interacting with ES7 from the minimally bound (structure 1 $_{\Delta}$ dII) to the
673 fully bound state (structure 6 $_{\Delta}$ dII) indicated with a prime (').

674 (D) RMSD (Å) of 18S rRNA for complexes labeled as in (E) compared to the minimally bound
675 state (structure 1 $_{\Delta}$ dII), color-coded as in the inset key. The angle formed between helix 33 (h33')
676 and helix 28 (h28') in structure 1 $_{\Delta}$ dII and helix 33 (h33'') in the labeled complex is also marked.

677 (E) Segmented maps for labeled complexes showing 40S subunit (yellow) and IRES (red)
678 organized in a putative sequence showing the minimally bound state (structure 1 $_{\Delta}$ dII), canonical
679 IRES binding (structure 6 $_{\Delta}$ dII) and the induction of opening of the head of the 40S subunit (structure
680 7 $_{\Delta}$ dII-9 $_{\Delta}$ dII).

681 See also Figure S4 and Table S4.

682

683 **Figure 3. IRES domain II is required for loading mRNA into the mRNA channel**

684 **(A)** RMSD (Å) of 18S rRNA for complexes labeled as in (B) compared to the minimally bound

685 state (structure $1_{\Delta\text{dII}}$), color-coded as in the inset key. The angle formed between helix 33 (h33')

686 and helix 28 (h28') in structure $1_{\Delta\text{dII}}$ and helix 33 (h33'') in the labeled complex is also marked.

687 **(B)** Segmented maps for labeled complexes showing 40S subunit (yellow), IRES (red), and eIF1A

688 (blue) organized in a putative sequence showing the minimally bound state (structure $1_{\Delta\text{dII}}$), fully

689 opened head of the 40S subunit (structure $9_{\Delta\text{dII}}$), binary complex (structure 10_{wt}), and the eIF1A-

690 containing ternary complex (structure 11_{wt}).

691 **(C)** Diagram of structures $1_{\Delta\text{dII}}$, $9_{\Delta\text{dII}}$, 10_{wt} and 11_{wt} showing the sequential loading of mRNA into

692 the mRNA channel.

693 **(D-F)** The mRNA channel spanning the entry and exit channels, A, P, and E sites viewed through

694 the ribosome head towards the body for the labeled complexes. The IRES (red), Coulomb potential

695 (blue mesh), and eIF1A (blue) are shown.

696 **(G)** Position of key nucleotides in the P site in structure 10_{wt} showing interactions between

697 incompletely loaded mRNA and C₁₆₉₈ resulting in C₁₇₀₁ sampling dual conformations near the (+2)

698 position.

699 **(H-I)** P site showing mRNA interactions for the (H) binary complex (structure 10_{wt}) and the (I)

700 eIF1A-containing ternary complex (structure 11_{wt}). 18S rRNA (yellow), eIF1A (blue), IRES

701 mRNA (red) with start codon (cyan) are all marked. The position of mRNA modelled in the 48S

702 cap-dependent IC (PDB: 6ZMW) is shown in grey.

703

704 **Figure 4. The HCV IRES•eIF2-containing 48S initiation complex.**

705 **(A)** Overview of the *wt* IRES eIF2-containing 48S IC (structure 12_{wt}).

706 **(B)** Contacts between eIF2 α and HCV IRES, Met-tRNA_i^{Met}, and 40S subunit.

707 **(C)** IRES domain II occupies multiple positions in the eIF2-containing 48S IC.

708 **(D)** Position of 18S rRNA in the open ternary complex (structure 11_{wt}) and eIF2-containing 48S

709 IC (structure 12_{wt}).

710 **(E-F)** The P site in the (E) ternary complex (structure 11_{wt}) and the (F) eIF2-containing 48S IC

711 (structure 12_{wt}) showing 18S rRNA (yellow), Met-tRNA_i^{Met} (magenta), eIF1A (blue), and IRES

712 mRNA (red) with the start codon (cyan) marked. **(E)** The position of mRNA in the cap-dependent

713 48S IC is marked (grey).

714 **(G-H)** Contacts between eS28 (salmon) and the IRES (red) in (G) the ternary complex (structure
715 11_{wt}) and (H) the eIF2-containing 48S IC (structure 12_{wt}).

716 **(I)** Global conformation of mRNA in the ternary complex (structure 11_{wt}) and the eIF2-containing
717 48S IC (structure 12_{wt}). The arrow indicates the extent of movement of eS28 between the binary
718 complex (structures 11_{wt}) and the eIF2-containing 48S IC complex (structure 12_{wt}).

719 See also Figure S5 and Table S5.

720

721 **Figure 5. The HCV IRES•eIF5B-containing 48S initiation complex**

722 **(A)** Overview of the *wt* IRES eIF5B-containing pre-48S IC (structure 14_{wt}).

723 **(B)** Overview of the *wt* IRES eIF5B-containing 48S IC (structure 15_{wt}).

724 **(C)** Changes to the position of P site tRNA depending on the presence of either eIF2 or eIF5B.
725 Upon binding of eIF5B, the T-arm, D-arm and acceptor stem of Met-tRNA_i^{Met} move by 15.6 Å
726 and 14° relative to their positions in the eIF2-containing 48S complex.

727 **(D)** Inset showing the conformation of tRNA acceptor stem loop, and contacts between eIF5B
728 domain IV and eIF1A. The conformation of the ASL is unchanged between the pre-48S IC
729 (eIF5B), and the 48S IC (eIF2 or eIF5B).

730 **(E)** Position of eIF5B and tRNA in the 48S and pre-elongation 80S ribosome complexes. eIF5B
731 undergoes relatively little movement between the 48S (green) and 80S stages (red) in the II, G,
732 and III domains, but domain IV translates and rotates (see F) causing movement in the tRNA
733 between the two complexes (magenta and orange respectively). Arrows show displacement for
734 labeled domains or components between the eIF5B-containing 48S IC and pre-elongation 80S
735 ribosome.

736 **(F)** The position of eIF5B domain IV in the 48S IC (green) would clash with 28S rRNA H89 and
737 uL16 in the 60S subunit. Upon binding of the 60S subunit, eIF5B domain IV (red) translates by
738 6.4 Å towards to the platform side of the 40S subunit and rotates by 30.9° causing the tRNA to
739 rotate by 12.4° and translate by 6.4 Å towards the head.

740 **(G-I)** P site for (G) eIF2-containing 48S IC (structure 12_{wt}), (H) eIF5B-containing pre-48S IC
741 (structure 14_{wt}), and (I) eIF5B-containing 48S IC (structure 15_{wt}) showing 18S rRNA (yellow),
742 Met-tRNA_i^{Met} (magenta), eIF1A (blue), and IRES mRNA (red) with the start codon (cyan) marked.

743 See also Figures S6-S7 and Tables S5-S6.

744

745 **Figure 6. Position of mRNA in the ribosomal P-site and codon-anticodon recognition.**

746 (A) Position of tRNA in the P site for the P_{OUT} complex (PDB: 7A09) (blue), 43S scanning
747 complex (PDB: 6ZMW) (yellow), and the pre-48S IC (structure 14_{wt}) (magenta). mRNA from the
748 43S scanning complex (green) and pre-48S IC (red) is shown.

749 (B) Contacts between tRNA, the initiation codon and the P site for the labeled complexes.

750 (C) The β 1- β 2 and β 3- β 4 loops of eIF1 bound as in the 43S scanning complex (PDB: 6ZMW)
751 would clash with the pre-48S IC position of Met-tRNA_i^{Met}.

752 See also Figure S7.

753

754 **Figure 7. The HCV IRES-mediated initiation pathway.**

755 Ribosomal complexes organized in a putative IRES-mediated initiation pathway. Maps are
756 segmented showing the 40S subunit (yellow), IRES (red), eIF1A (blue), Met-tRNA_i^{Met} (magenta),
757 and eIF2 or eIF5B (green).

758

759

760

761

762

763

764

765

766

767

768

769

770

771

772

773

774

775

776 **SUPPLEMENTARY FIGURE LEGENDS**

777

778 **Figure S1. Classification of HCV IRES containing ribosomal complexes, related to Figure 1.**

779 (A-D) Example micrographs for (A) the *wt* eIF2-containing sample, (B) the *wt* IRES eIF5B-
780 containing sample, (C) the Δ dII IRES eIF2-containing sample, and (D) the Δ dII IRES eIF5B-
781 containing sample. Further details in Table S2. Scale bar 2000 Å.

782 (E) Example 2D classification results for the *wt* IRES eIF2-containing sample.

783 (F-G) Classification scheme for (F) *wt* IRES and (G) Δ dII IRES containing samples. For full details
784 regarding classification see methods. Final maps are colored showing the 40S subunit (yellow),
785 IRES (red), eIF1A (blue), Met-tRNA_i^{Met} (magenta), and initiation factors eIF2 or eIF5B (green).
786 Full details for complexes are available in Table S3 (structures 1 $_{\Delta}$ dII-15 $_{wt/\Delta}$ dII), Table S5 (16 $_{wt}$ -28 $_{wt}$),
787 and Table S7 (structures 29 $_{wt}$ -46 $_{\Delta}$ dII).

788

789 **Figure S2. Local resolution, related to Figure 1.**

790 (A) Local resolution of labeled HCV IRES complexes.

791 (B) Central slice of each complex.

792 Local resolution values and filtered maps can be found under EMDB ascension codes for each
793 structure (see Table S3).

794

795 **Figure S3. Example densities, related to Figure 1.**

796 (A) Domain IIId (red) and ES7 (yellow) for the pre-48S IC (structure 14 $_{wt}$).

797 (B) Domain IIId (red) and ES7 (yellow) for the minimally bound complex (structure 1 $_{\Delta}$ dII)

798 (C) Contact between domain IIIa/IIIc (red) and riboprotein eS27 (magenta) in the ternary complex
799 (structure 12 $_{wt}$).

800 (D) eIF2 alpha helix 1 in the *wt* IRES 48S IC (structure 12 $_{wt}$), top, and the Δ dII IRES 48S IC
801 (structure 12 $_{\Delta}$ dII), bottom.

802 (E) eIF5B alpha helix 12 in the eIF5B-containing pre-48S IC (structure 14 $_{wt}$), top, and the 48S IC
803 (structure 15 $_{wt}$), bottom.

804 (F) eIF1A example densities from the eIF5B-containing pre-48S IC (structure 14 $_{wt}$), left, and the
805 eIF2-containing 48S IC (structure 12 $_{wt}$), right.

806 **(G)** Initiation codon (red) and tRNA anticodon (magenta) for all complexes where mRNA is
807 present in the P site. Diagram shows identity of nucleotides and hydrogen bonds for tRNA and
808 initiation codon bases in each accompanying figure.

809

810 **Figure S4. Interactions between HCV IRES and 40S ribosomal subunit for all complexes,**
811 **related to Figures 1 and 2.**

812 Contacts between ribosomal proteins (red), 18S rRNA (yellow), and the AUG codon (blue) are
813 marked. Labels refer to ribosomal proteins and elements of 18S rRNA, and to domains of the
814 IRES. Complexes assembled using the Δ dII IRES show the deleted domain marked in red. Also
815 see Table S4 for more details.

816

817 **Figure S5. eIF2 related supplement, related to Figure 4.**

818 **(A)** Overview of the Δ dII IRES eIF2-containing 48S initiation complex (structure 12 $_{\Delta$ dII}).

819 **(B-C)** Presence of Domain II in the E site causes the head of the 40S subunit to open. (B) Position
820 of 18S rRNA in the open ternary complex (structure 11 $_{wt}$) (orange), *wt* IRES eIF2-containing 48S
821 IC (structure 12 $_{wt}$) (yellow), and Δ dII IRES eIF2-containing 48S IC (structure 12 $_{\Delta$ dII}) (magenta).

822 **(C)** Position of 18S rRNA in the open ternary complex (structure 11 $_{wt}$) (orange), *wt* IRES w/o eIF2
823 48S IC (structure 13 $_{wt}$) (yellow), and Δ dII IRES w/o eIF2 48S IC (structure 13 $_{\Delta$ dII}) (magenta).

824 Measured angle between 18S rRNA h33 and h28 in the ternary complex (denoted with ') to h33 in
825 the *wt* IRES complex (denoted with '') shown for (C-D).

826 **(D)** Unsharpened maps for the *wt* IRES eIF2-containing 48S IC (structure 12 $_{wt}$), left, and the Δ dII
827 IRES eIF2-containing 48S IC (structure 12 $_{\Delta$ dII>), right. Comparison to canonical cap-dependent
828 initiation complexes (PDB: 6YAL) identifies the presence of eIF2 γ (cyan).

829 **(E)** The position and conformation of mRNA (magenta) and the eIF2 α -subunit for the *wt* IRES
830 eIF2-containing 48S IC (structure 12 $_{wt}$, green) and the Δ dII IRES eIF2-containing 48S IC
831 (structure 12 $_{\Delta$ dII}) (orange) is identical.

832 **(F)** Maps showing that domain II occupies multiple positions in the *wt* IRES eIF2-containing 48S
833 IC.

834 **(G-J)** Diagram of P site for the (G) IRES binary complex (structure 6 $_{\Delta$ dII>), **(H)** P site for pre-48S
835 IC (structure 14 $_{wt}$), **(I)** P site for eIF2-containing 48S IC (structure 12 $_{wt}$), and **(J)** P site for eIF5B-

836 containing 48S IC (structure 15_{wt}). Ribosomal proteins and 18S rRNA (yellow), mRNA (red),
837 tRNA (white), and eIF2 (green) are shown.

838

839 **Figure S6, related to Figure 5.**

840 **(A)** Overview of the ΔdII IRES eIF5B-containing 48S initiation complex (structure 15_{ΔdII}).

841 **(B)** Maps showing that domain II occupies multiple positions in the *wt* IRES eIF5B-containing
842 48S IC.

843 **(C)** Position of 18S rRNA in the *wt* IRES pre-48S IC (structure 14_{wt}) (orange), *wt* IRES eIF5B-
844 containing 48S IC (structure 15_{wt}) (magenta), and ΔdII IRES eIF5B-containing 48S IC (structure
845 15_{ΔdII}) (yellow). Measured angle between 18S rRNA h33 and h28 in the eIF5B-containing 48S IC
846 (denoted with ') to h33 in the pre-48S IC (denoted with "').

847 **(D)** Global position of eIF5B bound to the intersubunit face of the 40S ribosomal subunit.
848 Interactions between 18S rRNA (yellow), uS12 (salmon), and eIF1A (blue) are shown.

849 **(E)** Coulomb potential for the GTP nucleotide in eIF5B G domain for pre-48S IC (structure 14_{wt}),
850 left, and 48S IC (structure 15_{wt}), right.

851 **(F)** Comparison of conformation of switch 1 in GTP (orange) and GDP (blue), and switch 2 in
852 GTP (magenta) and GDP (yellow) conformations from the *C. thermophilum* G domain (grey)
853 (PDB: 4NCN). Conformational changes in domain II seen in the *O. cuniculus* 48S IC state (green)
854 and the *S. cerevisiae* pre-elongation 80S state (red) (PDB: 6WOO).

855 **(G)** Domain alignment between *O. cuniculus* pre-48S IC (structure 14_{wt})/48S IC (structure 15_{wt},
856 green) and *S. cerevisiae* eIF5B from the pre-elongation 80S (red) (PDB: 6WOO). Position of G
857 domain switch 1 (magenta) and switch 2 (orange) are marked

858

859 **Figure S7, related to Figures 5 and 6.**

860 **(A)** Structure of the *O. cuniculus* eIF5B G domain (PDB: 4UJD) bound to the pre-elongation 80S
861 ribosome (yellow) compared to the *O. cuniculus* pre-48S IC (structure 14_{wt}, green).

862 **(B)** Structure of the *O. cuniculus* eIF5B G domain in the pre-48S IC (structure 14_{wt}) (green).

863 **(C)** Structure of the *C. thermophilum* eIF5B G domain (PDB: 4NCN) (blue) compared to the *O.*
864 *cuniculus* eIF5B G domain bound to the pre-48S IC (structure 14_{wt}) (green).

865 **(D)** Structure of the *S. cerevisiae* eIF5B G domain (PDB: 6WOO) bound to the pre-elongation 80S
866 ribosome (red) compared to the *O. cuniculus* pre-48S IC (structure 14_{wt}) (green).

867 **(E-F)** Contacts between eS28 (salmon) and the HCV IRES (red) in the (E) pre-48S IC (structure
868 14_{wt}) and (F) 48S IC (structure 15_{wt}).

869 **(G)** Distance between P_{OUT} tRNA (PDB: 7A09) and the initiation codon in ternary complex
870 (structure 11_{wt})

871 **(H)** Contacts between tRNA and the P site for the eIF2-containing 48S IC.

872

873 **Table S1. Sample composition, related to Figure 1.**

874 **Table S2. Data collection statistics, related to Figure 1.**

875 **Table S3. Refinement and validation statistics, related to Figure 1.**

876 **Table S4. Contacts between the HCV IRES and 40S subunit, related to Figure 2.** Distances
877 below 3.5 Å are marked as ‘yes’, between 3.5-4.5 Å are marked as ‘weak’, and above 4.5 Å marked
878 as ‘no’.

879 **Table S5. Maps showing HCV IRES domain II movement, related to Figures 4 and 5.**

880 **Table S6. Contacts between eIF5B and the 40S subunit, related to Figure 5.**

881 **Table S7. Additional maps produced during data processing, related to Figure 1 and S1.**

882

883

884

885

886

887

888

889

890

891

892

893

894

895

896

897

898 **STAR Methods**

899 **Resource availability**

900

901 **Materials availability**

902 Requests for materials and additional information can be directed to Dr. Tatyana Pestova
903 (Tatyana.Pestova@downstate.edu;) or Dr. Joachim Frank (jf2192@cumc.columbia.edu).

904

905 **Data availability**

906 Primary models and maps (Table S3) reported in this study were deposited in the Protein
907 Data Bank (PDB) and Electron Microscopy Data Bank (EMDB) under the following accession
908 codes: structure $1_{\Delta\text{dII}}$ (PDB: XXXX; EMD-XXXX), structure $2_{\Delta\text{dII}}$ (PDB: XXXX; EMD-XXXX),
909 structure $3_{\Delta\text{dII}}$ (PDB: XXXX; EMD-XXXX), structure $4_{\Delta\text{dII}}$ (PDB: XXXX; EMD-XXXX),
910 structure $5_{\Delta\text{dII}}$ (PDB: XXXX; EMD-XXXX), structure $6_{\Delta\text{dII}}$ (PDB: XXXX; EMD-XXXX),
911 structure $7_{\Delta\text{dII}}$ (PDB: XXXX; EMD-XXXX), structure $8_{\Delta\text{dII}}$ (PDB: XXXX; EMD-XXXX),
912 structure $9_{\Delta\text{dII}}$ (PDB: XXXX; EMD-XXXX), structure 10_{wt} (PDB: XXXX; EMD-XXXX),
913 structure 11_{wt} (PDB: XXXX; EMD-XXXX), structure 12_{wt} (PDB: XXXX; EMD-XXXX),
914 structure $12_{\Delta\text{dII}}$ (PDB: XXXX; EMD-XXXX), structure 13_{wt} (PDB: XXXX; EMD-XXXX),
915 structure $13_{\Delta\text{dII}}$ (PDB: XXXX; EMD-XXXX), structure 14_{wt} (PDB: XXXX; EMD-XXXX),
916 structure 15_{wt} (PDB: XXXX; EMD-XXXX), and structure $15_{\Delta\text{dII}}$ (PDB: XXXX; EMD-XXXX).
917 For each entry half maps, the mask used for post processing, Fourier correlation curve, and local
918 resolution maps have been deposited as additional files.

919 Additional maps (table S5) showing the movement of HCV IRES domain II were deposited
920 in the EMDB under the following accession codes: structure 16_{wt} (EMD-XXXX), structure 17_{wt}
921 (EMD-XXXX), structure 18_{wt} (EMD-XXXX), structure 19_{wt} (EMD-XXXX), structure 20_{wt}
922 (EMD-XXXX), and structure 21_{wt} (EMD-XXXX), structure 22_{wt} (EMD-XXXX), structure 23_{wt}
923 (EMD-XXXX), structure 24_{wt} (EMD-XXXX), structure 25_{wt} (EMD-XXXX), structure 26_{wt}
924 (EMD-25555), structure 27_{wt} (EMD-XXXX), and structure 28_{wt} (EMD-XXXX). For each entry
925 half maps, the mask used for post processing, and Fourier correlation curve have been deposited
926 as additional files.

927 Maps obtained during data processing (Table S7) from particle stacks that were
928 compositionally and conformationally identical that were later combined were deposited in the

929 EMDB under the following accession codes: structure 29_{wt} (EMD-XXXX), structure 30_{wt} (EMD-
930 XXXX), structure 31_{ΔdII} (EMD-XXXX), and structure 32_{ΔdII} (EMD-XXXX). For each entry half
931 maps, the mask used for post processing, and Fourier correlation curve have been deposited as
932 additional files.

933 Consensus maps (Table S7) that were used for focused classification were deposited in the
934 EMDB under the following accession codes: structure 33_{ΔdII} (EMD-XXXX), structure 34_{ΔdII}
935 (EMD-XXXX), structure 35_{wt} (EMD-XXXX), structure 36_{wt} (EMD-XXXX), structure 37_{ΔdII}
936 (EMD-XXXX), structure 38_{wt} (EMD-XXXX), structure 39_{wt} (EMD-XXXX), and structure 40_{ΔdII}
937 (EMD-XXXX). Other high-resolution maps obtained during classification were deposited in the
938 EMDB under the following accession codes: structure 41_{wt} (EMD-XXXX), structure 42_{wt} (EMD-
939 XXXX), structure 43_{wt} (EMD-XXXX), structure 44_{wt} (EMD-XXXX), structure 45_{wt} (EMD-
940 XXXX), and structure 46_{ΔdII} (EMD-XXXX). For each entry half maps, the mask used for post
941 processing, mask used for focused classification, and the Fourier correlation curve have been
942 deposited as additional files.

943

944 **Method details**

945 **Plasmids**

946 Vectors for expression of His₆-tagged eIF1A (Pestova et al., 1998a) and *Escherichia coli*
947 methionyl tRNA synthetase (Lomakin et al., 2006) have been described. The plasmid HCV-
948 MSTN-Stop (Hashem et al., 2013) containing HCV Type 1 nt. 40–375 was used for transcription
949 of mRNA containing the *wt* HCV IRES. A derivative for transcription of HCV IRES lacking
950 domain II (containing HCV nt. 125–375) was made by GenScript Corp. (Piscataway, NJ). The
951 HCV plasmids were linearized by BamHI, and mRNAs were transcribed using T7 RNA
952 polymerase (Thermo Scientific).

953

954 **Purification of factors, ribosomal subunits and aminoacylation of tRNA**

955 Native mammalian 40S subunits, eIF2, eIF3 and eIF5B were purified from rabbit
956 reticulocyte lysate (RRL) (Green Hectares), as described (Pisarev et al., 2007). Recombinant
957 eIF1A and *Escherichia coli* methionyl tRNA synthetase were expressed and purified from *E.*
958 *coli* as described (Pisarev et al., 2007).

959 For purification of native rabbit total tRNA, 200 ml RRL were centrifuged at 45,000 rpm
960 for 4.5 h in a Beckman 50.2 Ti rotor at 4°C in order to pellet polysomes. The supernatant was
961 dialyzed overnight against buffer A (20 mM Tris [pH 7.5], 4 mM MgCl₂, 250 mM KCl, 2 mM
962 DTT) and applied to a DE52 (Whatman) column equilibrated with buffer A. The tRNA was eluted
963 with buffer B (20 mM Tris [pH 7.5], 3 mM MgCl₂, 700 mM NaCl, 2 mM DTT) and precipitated
964 overnight with 2.5 volumes of ethanol at -80°C. The precipitate was centrifuged at 13,000 rpm for
965 15 minutes and resuspended in 5 ml buffer C (100 mM Tris [pH 7.5], 5 mM MgCl₂), phenol-
966 chloroform (pH 4.7) extracted and precipitated again with 0.3 M NaOAc and 2.5 volumes of
967 ethanol. To isolate tRNA, the pellet was dissolved and subjected to gel filtration on a Superdex 75
968 column (Pestova and Hellen, 2001). Purified total tRNA was aminoacylated using *E. coli*
969 methionyl tRNA synthetase (to obtain Met-tRNA_i^{Met}) as described (Pisarev et al., 2007).

970

971 **Assembly of ribosomal complexes**

972 To form 48S initiation complexes, 7 pmol HCV IRES mRNA (*wt* or Δ domain II mutant)
973 were incubated with 3.5 pmol 40S subunits, 10 pmol eIF1A, 4.5 pmol eIF3, total native rabbit
974 tRNA containing 3.5 pmol Met-tRNA_i^{Met}, and 6 pmol eIF2 or 10 pmol eIF5B in 40 μ l buffer D
975 (20 mM Tris [pH 7.5], 100 mM KAc, 2.5 mM MgCl₂, 2 mM DTT, 0.25 mM spermidine, 1 mM
976 ATP and 0.2 mM GTP) for 10 minutes at 37°C. The obtained complexes (containing 87.5 nM 40S
977 subunits) were applied directly onto grids without dilution.

978

979 **Grid preparation and electron microscopy**

980 Gold foil grids were prepared from Quantifoil gold mesh grids (Passmore and Russo,
981 2016). Initially, Quantifoil R0.6/1.0 300 mesh gold grids (Quantifoil Micro Tools GmbH) were
982 visually inspected to check for uniformity and intactness of the Quantifoil layer and then placed
983 into an Auto 306 Turbo Vacuum Coater (Edwards Vacuum) at a pressure of 10³ Pa and then gold
984 wire (Ted Pella, Inc) was evaporated for approximately 8 minutes to create a 500 Å layer.
985 Deposition thickness was determined using the inbuilt film thickness monitor. To remove the
986 underlying Quantifoil carbon foil layer the grids were then treated with plasma using a Gatan
987 Solarus 950 (Gatan Inc) operated at 25 W for 4 minutes with an argon/oxygen gas mixture.

988 To prepare hydrophilic grids, 30 minutes prior to sample application, grids were treated
989 with plasma using a Gatan Solarus 950 (Gatan Inc) operated at 25W for 25 seconds with a

990 hydrogen/oxygen gas mixture. These grids were then transferred to the environmental chamber of
991 a Vitrobot Mark IV (Thermo Fisher Scientific) maintained at 4°C and 100% humidity. Here 3 μ L
992 of sample were applied and then blotted for 4 seconds with blot force 3 before immediate plunging
993 into an a cooled (77K) ethane-propane mixture (Tivol et al., 2008) and then transferred to liquid
994 nitrogen. Selected grids were screened to confirm sample composition and ice thickness using a
995 Tecnai F20 electron microscope (Thermo Fisher Scientific) equipped with a field emission gun
996 (FEG) operating at 200kV and a K2 summit direct electron detector (Gatan, Inc).

997 After screening grids from each sample, data collection was performed on a Tecnai Polara
998 F30 (Thermo Fisher Scientific) equipped with an FEG operating at 300 kV and a K3 direct electron
999 detector (Gatan, Inc). Movies were collected at a nominal magnification of 52,000 \times and defocus
1000 range of -0.5 to -2.5 μ m in counting mode with a pixel size of 0.95 $\text{\AA}/\text{pixel}$ using the automated
1001 collection software Leginon (Potter et al., 1999; Carragher et al., 2000; Suloway et al., 2005). Each
1002 movie consisted of 40 frames recorded over 4 seconds with a total dose of 70.9 $e^-/\text{\AA}^2$. Due to
1003 sample conditions the 40S ribosome may enter a preferred orientation and so portions of the data
1004 were collected with a 30° stage tilt (Table S2). For the *wt* IRES eIF2-containing sample 14,815
1005 micrographs (14,815 at 30° stage tilt) were collected over 2 sessions, for the *wt* IRES eIF5B-
1006 containing sample 27,263 micrographs (20,509 at 30° stage tilt) were collected over 4 sessions,
1007 for the Δ dII IRES eIF2-containing sample 22,735 micrographs (17,695 at 30° stage tilt) were
1008 collected over 3 sessions, and for the Δ dII IRES eIF5B-containing sample 13,809 micrographs
1009 (13,809 at 30° stage tilt) were collected over 2 sessions (Table S2). Optical groups of micrographs
1010 with similar beam tilt values were identified using k-means clustering on the image shift values
1011 recorded by the microscope during data collection.

1012

1013 **Image processing**

1014 Gain references for each session were produced by visually screening ~1000 micrographs
1015 to remove images that contained gold foil and then summing them using *cisTEM sum_all_tifs*
1016 (Grant et al., 2018). Movies were then aligned using MotionCor2 (Zheng et al., 2017) with dose
1017 weighting of 1.77 $e^-/\text{\AA}^2/\text{frame}$ and local patch correction with 8 \times 5 patches. Initial CTF parameters
1018 were estimated using CTFFIND4 (Rohou and Grigorieff, 2015). Particle locations were identified
1019 using Topaz version 0.2.3 (Bepler et al. 2019) by initially downscaling all micrographs by 8 \times and
1020 then using the Topaz general model to identify particles. Particles with a confidence score below

1021 0 were removed and the remaining positions rescaled for subsequent processing in Relion 3.1
1022 (Scheres, 2012; 2016; Zivanov et al., 2018; 2019).

1023 Initially, we identified 2,183,185 particles for the *wt* IRES eIF2-containing sample
1024 (147 particles per micrograph), 1,133,335 particles for the *wt* IRES eIF5B-containing sample
1025 (42 particles per micrograph), 2,213,826 particles for the Δ dII IRES eIF2-containing sample
1026 (97 particles per micrograph), and 1,459,506 particles for the Δ dII IRES eIF5B-containing sample
1027 (106 particles per micrograph). Particle locations were extracted from micrographs into
1028 downsampled boxes of 100×100 pixels (at 3.8 \AA/pixel) to speed initial classification. This
1029 corresponds to 400×400 -pixel boxes (at 0.95 \AA/pixel) without downsampling. 25 iterations of 2D
1030 classification were performed to identify incorrectly picked particles, contamination, and other
1031 particles that were unable to be correctly aligned (e.g., due to poor SNR). Particles that were
1032 selected for removal were subjected to additional 2D classification to confirm that they did not
1033 contain clear 40S ribosome particles.

1034 After initial screening of the 2D classification data the remaining particles for each sample
1035 were 1,201,923 particles for the *wt* IRES eIF2-containing sample (81 particles per micrograph),
1036 736,700 particles for the *wt* IRES eIF5B-containing sample (36 particles per micrograph),
1037 1,484,658 particles for the Δ dII IRES eIF2-containing sample (84 particles per micrograph), and
1038 1,119,610 particles for the Δ dII IRES eIF5B-containing sample (81 particles per micrograph). For
1039 each sample, all particles were refined into a single model which was used to estimate the defocus
1040 values on a per-particle basis, followed by an additional refinement step, and then 3D classification
1041 without alignment into 10 classes for 25 iterations. This initial 3D classification was used to
1042 identify the major conformational states present in each sample, as well as further removal of poor-
1043 quality particles. For the *wt* IRES eIF2-containing sample we identified 580,938 particles in the
1044 closed state, 176,793 particles in the open state, and removed 444,192 particles. For the *wt* IRES
1045 eIF5B-containing sample we identified 378,325 open state, 360,338 closed state, and removed
1046 58,037 particles. For the Δ dII IRES eIF5B-containing sample we identified 883,893 particles in
1047 the closed state, and removed 62,455 particles. For the Δ dII IRES eIF2-containing sample we
1048 identified 615,125 particles in the closed state, 198,920 particles in the intermediate-open state,
1049 and removed 670,433 particles. All particles that were selected for removal were subjected to
1050 additional 2D classification and 3D refinement steps to confirm that they did not contain 40S
1051 ribosome complexes.

1052

1053 **General processing pathway**

1054 All particles were re-extracted at full-size (400×400-pixel box, 0.95 Å/pixel) and
1055 underwent iterations of 3D refinement, following by anisotropic magnification correction, defocus
1056 refinement, and beam tilt estimation. Multiple rounds of 3D classification (25 iterations, without
1057 alignment) were used to progressively remove poor quality particles. After each round of CTF
1058 refinement each particle stack underwent 3D refinement and was checked for increase in resolution
1059 and visual improvement of map density. Once CTF refinement no longer improved map quality,
1060 particle polishing using all frames was performed and then iterations of CTF refinement as outline
1061 above were completed. Focused classification on consensus maps was performed to isolate desired
1062 conformational or compositional states (see below).

1063

1064 ***wt* IRES eIF2-containing sample**

1065 After 3D classification the consensus map of closed 40S ribosome particles (Table S7)
1066 from the *wt* IRES eIF2-containing sample contained 530,720 particles at 3.1 Å resolution (structure
1067 36_{wt}; EMD-XXXX) underwent focused classification by enclosing Met-tRNA_i^{Met} and the eIF2α
1068 subunit in a mask. Iterations of focused classification were able to produce two high quality classes
1069 of either the eIF2-containg 48S IC with 46,904 particles at 3.6 Å resolution (structure 12_{wt};
1070 PDB: XXXX; EMD-XXXX) and the 48S IC w/o eIF2 with 15,598 particles at 4.4 Å resolution
1071 (structure 13_{wt}; PDB: XXXX; EMD-XXXX). An additional class of the eIF2-containg 48S IC
1072 lacking eIF1A with 45,571 particles at 3.6 Å resolution (structure 45_{wt}; EMD-XXXX) was
1073 obtained. Extensive classification of the remaining 422,647 particles produced maps that showed
1074 the 40S ribosome bound to eIF2 and/or Met-tRNA_i^{Met} but with a low resolution, or the ribosome
1075 lacking both factors.

1076 To determine the positions that IRES domain II occupies the region around domain II was
1077 masked and classified into 10 classes over 25 iterations without alignment. Six classes were able
1078 to be clearly resolved showing IRES domain II sampling different positions around the ribosome
1079 head. Class 1 containing 41,393 particles at 3.8 Å resolution (structure 16_{wt}; EMD-XXXX), class
1080 2 containing 39,148 particles at 3.8 Å resolution (structure 17_{wt}; EMD-XXXX), class 3 containing
1081 49,034 particles at 3.7 Å resolution (structure 18_{wt}; EMD-XXXX), class 4 containing 66,090
1082 particles at 3.6 Å resolution (structure 19_{wt}; EMD-XXXX), class 5 containing 24,190 particles at

1083 3.9 Å resolution (structure 20_{wt}; EMD-XXXX), and class 6 containing 36,155 particles at 3.8 Å
1084 resolution (structure 21_{wt}; EMD-XXXX). Extensive classification of the remaining 274,710
1085 particles could not further resolved additional positions of domain II.

1086 After extracting at full size the consensus map of the open 40S ribosome particles (Table
1087 S7) from the *wt* IRES eIF2-containing sample contained 176,793 particles at 3.8 Å resolution
1088 (structure 29_{wt}; EMD-XXXX).

1089

1090 ***wt* IRES eIF5-containing sample**

1091 The consensus map of closed 40S ribosome particles (Table S7) from the *wt* IRES eIF5B-
1092 containing sample contained 360,338 particles at 3.4 Å resolution (structure 39_{wt}; EMD-XXXX)
1093 underwent focused classification by enclosing eIF5B in a mask. This could be classified into three
1094 high-resolution classes of the eIF5B-containing 48S IC eIF5B: one containing 133,782 particles
1095 at 3.7 Å resolution (structure 15_{wt}; PDB: XXXX; EMD-XXXX), one containing 109,025 particles
1096 at 3.7 Å resolution (structure 41_{wt}; EMD-XXXX), and one containing 55,367 at 3.8 Å resolution
1097 (structure 42_{wt}; EMD-XXXX). The remaining 62,164 particles showed the 48S IC at 3.9 Å
1098 resolution but the occupancy of eIF5B was lower (structure 43_{wt}; EMD-XXXX).

1099 To determine the positions that IRES domain II occupies the region around domain II was
1100 masked and classified into 10 classes over 25 iterations without alignment. Seven classes were
1101 able to be resolved showing IRES domain II sampling different positions around the ribosome
1102 head. Class 1 containing 20,138 particles at 5.0 Å resolution (structure 22_{wt}; EMD-XXXX), class
1103 2 containing 11,082 particles at 5.4 Å resolution (structure 23_{wt}; EMD-XXXX), class 3 containing
1104 16,584 particles at 5.2 Å resolution (structure 24_{wt}; EMD-XXXX), class 4 containing 16,217
1105 particles at 4.9 Å resolution (structure 25_{wt}; EMD-XXXX), class 5 containing 8,102 particles at
1106 6.0 Å resolution (structure 26_{wt}; EMD-XXXX), class 6 containing 13,152 particles at 5.3 Å
1107 resolution (structure 27_{wt}; EMD-XXXX), and class 7 containing 7,029 particles at 6.2 Å resolution
1108 (structure 28_{wt}; EMD-XXXX). Extensive classification of the remaining 268,034 particles could
1109 not further resolved the position of domain II.

1110 The consensus map of open 40S ribosome particles (Table S7) from the *wt* IRES eIF5B-
1111 containing sample was classified into two classes: a consensus eIF5B-containing pre-48S IC with
1112 199,047 particles at 3.6 Å (structure 38_{wt}; EMD-XXXX) and the open binary complex with
1113 147,309 particles at 4.1 Å resolution (structure 30_{wt}; EMD-XXXX). The 31,969 remaining

1114 particles were subjected to 3D classification but did now contain high-quality classes. The
1115 consensus map of the eIF5B containing pre-48S IC (structure 38_{wt}) was masked around eIF5B and
1116 focused classification produced two classes, one with 60,578 particles at 3.8 Å (structure 14_{wt};
1117 PDB: XXXX; EMD-XXXX), and a lower-resolution map from 29,072 particles at 4.2 Å (structure
1118 44_{wt}; EMD-XXXX).

1119

1120 **ΔdII IRES eIF2-containing sample**

1121 The consensus map of closed 40S ribosome particles (Table S7) from the ΔdII IRES eIF2-
1122 containing sample contained 615,195 particles at 3.3 Å resolution (structure 37_{ΔdII}; EMD-25596)
1123 underwent focused classification by enclosing Met-tRNA_i^{Met} and the eIF2α subunit in a mask.
1124 Iterations of focused classification were able to produce two high quality classes of either the eIF2-
1125 containg 48S IC (structure 12_{ΔdII}; PDB: XXXX; EMD-XXXX), and the 48S IC w/o eIF2 (structure
1126 13_{ΔdII}; PDB: XXXX; EMD-XXXX). An additional class of 147,713 particles at 3.6 Å (structure
1127 46_{ΔdII}; EMD-XXXX) showed the 48S IC but with very poor density for eIF2. Extensive
1128 classification of the remaining 348,071 particles did not produced any high-quality maps. The
1129 consensus map of the intermediate conformation 40S ribosome particles (Table S7) from the ΔdII
1130 IRES eIF2-containing sample had 198,920 particles at 3.5 Å resolution (structure 31_{ΔdII}; EMD-
1131 25590).

1132

1133 **ΔdII IRES eIF5B-containing sample**

1134 3D classification of the closed state eIF5B-containing 40S ribosome produced three classes
1135 that were processed further (Figure S1G; Table S7). The consensus map of closed 40S ribosome
1136 particles (Table S7) from the ΔdII IRES eIF5B-containing sample contained 148,763 particles at
1137 3.4 Å resolution (structure 40_{ΔdII}; EMD-XXXX) and underwent focused classification by
1138 enclosing eIF5B in a mask. Iterations of focused classification were able to produce one high
1139 quality class of the eIF5B-containg 48S IC (structure 15_{ΔdII}; PDB: XXXX; EMD-XXXX).
1140 Classification of the remaining 99,239 particles produced maps at either low resolution or lacking
1141 eIF5B. The consensus map showing the closed 40S ribosome with multiple HCV IRES states
1142 (Table S7) had 346,516 particles at 3.6 Å resolution (structure 33_{ΔdII}; EMD-XXXX). A mask was
1143 prepared around IRES domains S1/S2/IIIe/IIIf and focused classification resolved six classes of
1144 the IRES in various association/dissociation states: (1) the early stage association between the

1145 IRES and 40S/IRES_{ΔdII} binary complex with 42,271 particles at 4.3 Å resolution (structure 1_{ΔdII};
1146 PDB: XXXX; EMD-XXXX), (2) the early stage association between the IRES and 40S/IRES_{ΔdII}
1147 binary complex with 28,684 particles at 4.6 Å resolution (structure 2_{ΔdII}; PDB: 7SYH; EMD-
1148 XXXX), (3) the early stage association between the IRES and 40S/IRES_{ΔdII} binary complex with
1149 24,545 particles at 4.5 Å resolution (structure 3_{ΔdII}; PDB: XXXX; EMD-XXXX), (4) the early
1150 stage association between the IRES and 40S/IRES_{ΔdII} binary complex with 27,043 particles at 4.8
1151 Å resolution (structure 4_{ΔdII}; PDB: XXXX; EMD-XXXX), (5) the early stage association between
1152 the IRES and 40S/IRES_{ΔdII} binary complex with 48,757 particles at 4.2 Å resolution (structure
1153 5_{ΔdII}; PDB: XXXX; EMD-XXXX), and (6) the canonically bound IRES 40S/IRES_{ΔdII} binary
1154 complex with 29,657 particles at 4.5 Å resolution (structure 6_{ΔdII}; PDB: XXXX; EMD-XXXX).
1155 The remaining 145,559 particles were classified into either low-resolution maps or with the 40S
1156 ribosome lacking the HCV IRES. The consensus map of the intermediate 40S ribosome particles
1157 (Table S7) from the ΔdII IRES eIF5B-containing sample had 287,087 particles at 4.5 Å resolution
1158 (structure 32_{ΔdII}; EMD-XXXX).

1159

1160 **Combining ΔdII IRES intermediate 40S ribosome particles and focused classification**

1161 Both eIF2-, and eIF5B-containing samples prepared on the ΔdII IRES yielded
1162 classes that showed the HCV IRES bound to the 40S ribosome where the head of the ribosome
1163 was in multiple states (structure 31_{ΔdII}-32_{ΔdII}). Both maps were visually inspected and showed high
1164 similarity (unsharpened maps a correlation of 0.9834, and after B-factor sharpening 0.9295). We
1165 combined these particles into a consensus map of 456,311 particles at 3.5 Å resolution (structure
1166 34_{ΔdII}; EMD-XXXX) that underwent focused classification of the entire head region of the
1167 ribosome that produced three classes: the closed 40S/IRES_{ΔdII} binary complex with 59,660
1168 particles at 4.8 Å resolution (structure 7_{ΔdII}; PDB: XXXX; EMD-XXXX), the intermediate-open
1169 40S/IRES_{ΔdII} binary complex with 144,252 particles at 4.0 Å resolution (structure 8_{ΔdII};
1170 PDB: XXXX; EMD-XXXX), and the open 40S/IRES_{ΔdII} binary complex with 46,095 particles at
1171 4.6 Å resolution (structure 9_{ΔdII}; PDB: XXXX; EMD-XXXX). The remaining 206,304 particles
1172 were classified into low resolution maps.

1173

1174 **Combining *wt* IRES open 40S ribosome particles and focused classification**

1175 Both eIF2-, and eIF5B-containing samples prepared on the *wt* IRES yielded classes that
1176 showed the HCV IRES bound to the 40S ribosome with IRES domain II inserted into the E site
1177 (structure 29_{wt}-30_{wt}). Both maps were visually inspected and showed high similarity (unsharpened
1178 maps correlation of 0.9945, and after B-factor sharpening 0.9464). We combined these particles
1179 into a consensus map of 324,102 particles at 3.3 Å resolution (structure 35_{wt}; EMD- XXXX) that
1180 underwent focused classification of eIF1A that produced two classes: the binary complex with
1181 119,320 particles at 3.8 Å resolution (structure 10_{wt}; PDB: XXXX; EMD-XXXX), and the ternary
1182 complex with 204,782 particles at 3.8 Å resolution (structure 11_{wt}; PDB: XXXX; EMD-XXXX).
1183

1184 **Model building, and refinement**

1185 For all data, where applicable, we were able to unambiguously fit the head and body of the
1186 40S (PDB: 6D9J; Pisareva et al. 2018), HCV IRES (PDB: 5FLX; Yamamoto et al. 2015), eIF1A
1187 (PDB: 4KZZ; Lomakin and Steitz 2013), tRNA (PDB: 5K0Y; Simonetti et al. 2016) eIF2α subunit
1188 (PDB: 6O85; Kenner et al. 2019), and eIF5B (PDB: 4UJD; Yamamoto et al. 2014). Initial model
1189 fitting was performed using UCSF Chimera v1.14 (Pettersen et al., 2004) with additional
1190 modelling in Coot (Emsley and Cowtan, 2004). For regions of eIF5B that did not have available
1191 models (e.g., Switch 1) model building was performed independently and then cross-checked for
1192 consistency. All models underwent one round of Phenix geometry minimization and multiple
1193 rounds of PHENIX real-space refinement (Adams et al., 2010; Afonine et al., 2018).
1194

1195 **Figures**

1196 All figures were prepared using UCSF Chimera v1.14 (Pettersen et al., 2004).
1197

1198 **Quantification and statistical analysis**

1199 Global resolution estimates were calculated using the 0.143 FSC criterion (Rosenthal and
1200 Henderson, 2003). Local resolution maps were calculated using Relion 3.1 (Scheres, 2012; 2016;
1201 Zivanov et al., 2018; 2019) using the B-factor determined during post processing and the
1202 Modulation transfer function (MTF) curve for the K3 camera at 300 kV provided by the
1203 manufacturer. (<https://www.gatan.com/techniques/cryo-em#MTF>). RMSD calculations for 18S
1204 rRNA chains were performed using Pymol (Schrödinger, 2015). Model validation for all models

1205 were calculated using PHENIX (Adams et al., 2010; Afonine et al., 2018) installed as part of the
1206 SBGrid package (Morin et al., 2013).

1207

1208

1209 REFERENCES

1210

1211 Acker, M.G., Shin, B.S., Dever, T.E., and Lorsch, J.R. (2006). Interaction between eukaryotic initiation factors 1A
1212 and 5B is required for efficient ribosomal subunit joining. *J. Biol. Chem.* 281, 8469-8475. [10.1074/jbc.M600210200](https://doi.org/10.1074/jbc.M600210200).

1213

1214 Adams, P.D., Afonine, P.V., Bunkóczki, G., Chen, V.B., Davis, I.W., Echols, N., Headd, J.J., Hung, L.W., Kapral, G.J.,
1215 Grosse-Kunstleve, R.W., McCoy, A.J., Moriarty, N.W., Oeffner, R., Read, R.J., Richardson, D.C., Richardson, J.S.,
1216 Terwilliger, T.C., Zwart, P.H. (2010). PHENIX: a comprehensive Python-based system for macromolecular structure
1217 solution. *Acta Crystallogr. D Biol. Crystallogr.* 66, 213-221. [10.1107/S0907444909052925](https://doi.org/10.1107/S0907444909052925).

1218

1219 Afonine, P.V., Poon, B.K., Read, R.J., Sobolev, O.V., Terwilliger, T.C., Urzhumtsev, A., and Adams, P.D. (2018).
1220 Real-space refinement in PHENIX for cryo-EM and crystallography. *Acta Crystallogr. D Struct. Biol.* 74, 531-544.
1221 [10.1107/S2059798318006551](https://doi.org/10.1107/S2059798318006551).

1222

1223 Angulo, J., Ulryck, N., Deforges, J., Chamond, N., Lopez-Lastra, M., Masquida, B., and Sargueil, B. (2016). LOOP
1224 IIId of the HCV IRES is essential for the structural rearrangement of the 40S-HCV IRES complex. *Nucleic Acids Res.*
1225 44, 1309-25. [10.1093/nar/gkv1325](https://doi.org/10.1093/nar/gkv1325).

1226

1227 Arhab, Y., Bulakhov, A.G., Pestova, T.V., and Hellen, C.U.T. (2020). Dissemination of internal ribosomal entry sites
1228 (IRES) between viruses by horizontal gene transfer. *Viruses* 12, 612. [10.3390/v12060612](https://doi.org/10.3390/v12060612).

1229

1230 Battiste, J.L., Pestova, T.V., Hellen, C.U., and Wagner, G. (2000). The eIF1A solution structure reveals a large RNA-
1231 binding surface important for scanning function. *Mol. Cell* 5, 109-119. [10.1016/s1097-2765\(00\)80407-4](https://doi.org/10.1016/s1097-2765(00)80407-4)

1232

1233 Bepler, T., Morin, A., Rapp, M., Brasch, J., Shapiro, L., Noble, A.J., and Berger, B. (2019). Positive-unlabeled
1234 convolutional neural networks for particle picking in cryo-electron micrographs. *Nat. Methods* 16, 1153-1160.
1235 10.1038/s41592-019-0575-8.

1236

1237 Boehringer, D., Thermann, R., Ostareck-Lederer, A., Lewis, J.D., and Stark, H. (2005). Structure of the hepatitis C
1238 virus IRES bound to the human 80S ribosome: remodeling of the HCV IRES. *Structure* 13, 1695-706.
1239 10.1016/j.str.2005.08.008.

1240

1241 Brito Querido, J., Sokabe, M., Kraatz, S., Gordiyenko, Y., Skehel, J.M., Fraser, C.S., and Ramakrishnan, V. (2020).
1242 Structure of a human 48S translational initiation complex. *Science* 369, 1220-1227. [10.1126/science.aba4904](https://doi.org/10.1126/science.aba4904).

1244 Carragher, B., Kisseberth, N., Kriegman, D., Milligan, R.A., Potter, C.S., Pulokas, J., and Reilein, A. (2000). Leginon:
1245 an automated system for acquisition of images from vitreous ice specimens. *J. Struct. Biol.* 132, 33-45.
1246 10.1006/jsbi.2000.4314.

1247

1248 de Breyne, S., Yu, Y., Pestova, T.V., and Hellen, C.U. (2008). Factor requirements for translation initiation on the
1249 Simian picornavirus internal ribosomal entry site. *RNA* 14, 367-380. [10.1261/rna.696508](https://doi.org/10.1261/rna.696508).

1250

1251 des Georges, A., Dhote, V., Kuhn, L., Hellen, C.U., Pestova, T.V., Frank, J., and Hashem, Y. (2015) Structure of
1252 mammalian eIF3 in the context of the 43S preinitiation complex. *Nature* 525, 491-495. [10.1038/nature14891](https://doi.org/10.1038/nature14891).

1253

1254 d'Imprima, E., Floris, D., Joppe, M., Sánchez, R., Grininger, M., and Kühlbrandt, W. (2019). Protein denaturation at
1255 the air-water interface and how to prevent it. *Elife* 8, e42747. [10.7554/elife.42747](https://doi.org/10.7554/elife.42747).

1256

1257 Easton, L.E., Locker, N., and Lukavsky, P.J. (2009). Conserved functional domains and a novel tertiary interaction
1258 near the pseudoknot drive translational activity of hepatitis C virus and hepatitis C virus-like internal ribosomal entry
1259 sites. *Nucleic Acids Res.* 37, 5537-5549. [10.1093/nar/gkp588](https://doi.org/10.1093/nar/gkp588).

1260

1261 Emsley, P., and Cowtan, K. (2004). Coot: model-building tools for molecular graphics. *Acta Crystallogr. D Biol.*
1262 *Crystallogr.* 60, 2126-2132. 10.1107/S0907444904019158.

1263

1264 Filbin, M.E., and Kieft, J.S. (2011). HCV IRES domain IIb affects the configuration of coding RNA in the 40S
1265 subunit's decoding groove. *RNA* 17, 1258-1273. [10.1261/rna.2594011](https://doi.org/10.1261/rna.2594011).

1266

1267 Fletcher, C.M., Pestova, T.V., Hellen, C.U., and Wagner, G. (1999). Structure and interactions of the translation
1268 initiation factor eIF1. *EMBO J.* 18, 2631-2637. [10.1093/emboj/18.9.2631](https://doi.org/10.1093/emboj/18.9.2631).

1269

1270 Glaeser, R.M. (2021). Preparing better samples for cryo-electron microscopy: Biochemical challenges do not end with
1271 isolation and purification. *Annu. Rev. Biochem.* 90, 451-474. [10.1146/annurev-biochem-072020-020231](https://doi.org/10.1146/annurev-biochem-072020-020231)

1272

1273 Grant, T., Rohou, A., and Grigorieff, N. (2018). *cis*TEM, user-friendly software for single-particle image
1274 processing. *Elife* 7, e35383. [10.7554/elife.35383](https://doi.org/10.7554/elife.35383).

1275

1276 Hashem, Y., des Georges, A., Dhote, V., Langlois, R., Liao, H.Y., Grassucci, R.A., Pestova, T.V., Hellen, C.U., and
1277 Frank, J. (2013). Hepatitis-C-virus-like internal ribosome entry sites displace eIF3 to gain access to the 40S subunit.
1278 *Nature* 503, 539-543. [10.1038/nature12658](https://doi.org/10.1038/nature12658).

1279

1280 Honda, M., Ping, L.H., Rijnbrand, R.C., Amphlett, E., Clarke, B., Rowlands, D., and Lemon, S.M. (1996). Structural
1281 requirements for initiation of translation by internal ribosome entry within genome-length hepatitis C virus RNA.
1282 *Virology* 222, 31-42. [10.1006/viro.1996.0395](https://doi.org/10.1006/viro.1996.0395).

1283

1284 Huang, B.Y., and Fernández, I.S. (2020). Long-range interdomain communications in eIF5B regulate GTP hydrolysis
1285 and translation initiation. *Proc. Natl. Acad. Sci. U.S.A.* 117, 1429-1437. [10.1073/pnas.1916436117](https://doi.org/10.1073/pnas.1916436117).

1286

1287 Hussain, T., Llácer, J.L., Fernández, I.S., Muñoz, A., Martín-Marcos, P., Savva, C.G., Lorsch, J.R., Hinnebusch, A.G.,
1288 and Ramakrishnan, V. (2014). Structural changes enable start codon recognition by the eukaryotic translation initiation
1289 complex. *Cell* 159, 597-607. [10.1016/j.cell.2014.10.001](https://doi.org/10.1016/j.cell.2014.10.001).

1290

1291 Hussain, T., Llácer, J.L., Wimberly, B.T., Kieft, J.S., and Ramakrishnan, V. (2016). Large-Scale Movements of IF3
1292 and tRNA during Bacterial Translation Initiation. *Cell* 167, 133-144.e13. [10.1016/j.cell.2016.08.074](https://doi.org/10.1016/j.cell.2016.08.074).

1293

1294 Jaafar, Z.A., Oguro, A., Nakamura, Y., and Kieft, J.S. (2016). Translation initiation by the hepatitis C virus IRES
1295 requires eIF1A and ribosomal complex remodeling. *Elife* 5, e21198. [10.7554/elife.21198](https://doi.org/10.7554/elife.21198).

1296

1297 Jackson, R.J., Hellen, C.U., and Pestova, T.V. (2010). The mechanism of eukaryotic translation initiation and
1298 principles of its regulation. *Nat. Rev. Mol. Cell. Biol.* 11, 113-127. [10.1038/nrm2838](https://doi.org/10.1038/nrm2838).

1299

1300 Ji, H., Fraser, C.S., Yu, Y., Leary, J., and Doudna, J.A. (2004). Coordinated assembly of human translation initiation
1301 complexes by the hepatitis C virus internal ribosome entry site RNA. *Proc. Natl. Acad. Sci. U.S.A.* 101, 16990-16995.
1302 [10.1073/pnas.0407402101](https://doi.org/10.1073/pnas.0407402101).

1303

1304 Jumper, J., Evans, R., Pritzel, A., Green, T., Figurnov, M., Ronneberger, O., Tunyasuvunakool, K., Bates, R., Žídek,
1305 A., Potapenko, A., Bridgland, A., Meyer, C., Kohl, S.A.A., Ballard, A.J., Cowie, A., Romera-Paredes, B., Nikolov,
1306 S., Jain, R., Adler, J., Back, T., Petersen, S., Reiman, D., Clancy, E., Zielinski, M., Steinegger, M., Pacholska, M.,
1307 Berghammer, T., Bodenstein, S., Silver, D., Vinyals, O., Senior, A.W., Kavukcuoglu, K., Kohli, P., Hassabis, D.
1308 (2021). Highly accurate protein structure prediction with AlphaFold. *Nature* 596, 583-589. [10.1038/s41586-021-03819-2](https://doi.org/10.1038/s41586-021-03819-2).

1310

1311 Kenner, L.R., Anand, A.A., Nguyen, H.C., Myasnikov, A.G., Klose, C.J., McGeever, L.A., Tsai, J.C., Miller-Vedam,
1312 L.E., Walter, P., and Frost, A. (2019). eIF2B-catalyzed nucleotide exchange and phosphoregulation by the integrated
1313 stress response. *Science* 364, 491-495. [10.1126/science.aaw2922](https://doi.org/10.1126/science.aaw2922).

1314

1315 Kieft, J.S., Zhou, K., Jubin, R., and Doudna, J.A. (2001). Mechanism of ribosome recruitment by hepatitis C IRES
1316 RNA. *RNA* 7, 194-206. [10.1017/s1355838201001790](https://doi.org/10.1017/s1355838201001790).

1317

1318 Kolupaeva, V.G., Pestova, T.V., and Hellen, C.U. (2000). An enzymatic footprinting analysis of the interaction of
1319 40S ribosomal subunits with the internal ribosomal entry site of hepatitis C virus. *J Virol.* 2000 Jul;74(14):6242-50.
1320 [10.1128/jvi.74.14.6242-6250.2000](https://doi.org/10.1128/jvi.74.14.6242-6250.2000).

1321

1322 Kratzat, H., Mackens-Kiani, T., Ameismeier, M., Potocnjak, M., Cheng, J., Dacheux, E., Namane, A., Berninghausen,
1323 O., Herzog, F., Fromont-Racine, M., Becker, T., and Beckmann, R. (2021). A structural inventory of native ribosomal
1324 ABCE1-43S pre-initiation complexes. *EMBO J.* 40, e105179. [10.1525/embj.2020105179](https://doi.org/10.1525/embj.2020105179).

1325

1326 Kuhle, B., and Ficner, R. (2014). eIF5B employs a novel domain release mechanism to catalyze ribosomal subunit
1327 joining. *EMBO J.* 33, 1177-1191. [10.1002/embj.201387344](https://doi.org/10.1002/embj.201387344).

1328

1329 Llacer, J.L., Hussain, T., Marler, L., Aitken, C.E., Thakur, A., Lorsch, J.R., Hinnebusch, A.G., and Ramakrishnan, V.
1330 (2015). Conformational Differences between Open and Closed States of the Eukaryotic Translation Initiation
1331 Complex. *Mol. Cell* 59, 399-412. [10.1016/j.molcel.2015.06.033](https://doi.org/10.1016/j.molcel.2015.06.033).

1332

1333 Locker, N., Easton, L.E., and Lukavsky, P.J. (2007). HCV and CSFV IRES domain II mediate eIF2 release during
1334 80S ribosome assembly. *EMBO J.* 26, 795-805. [10.1038/sj.emboj.7601549](https://doi.org/10.1038/sj.emboj.7601549).

1335

1336 Lomakin, I.B., and Steitz, T.A. (2013). The initiation of mammalian protein synthesis and mRNA scanning
1337 mechanism. *Nature* 500, 307-311. [10.1038/nature12355](https://doi.org/10.1038/nature12355).

1338

1339 Lomakin, I.B., Shirokikh, N.E., Yusupov, M.M., Hellen, C.U., and Pestova, T.V. (2006). The fidelity of translation
1340 initiation: reciprocal activities of eIF1, IF3 and YciH. *EMBO J.* 25, 196-210. [10.1038/sj.emboj.7600904](https://doi.org/10.1038/sj.emboj.7600904).

1341

1342 Maag, D., Fekete, C.A., Gryczynski, Z., and Lorsch, J.R. (2005). A conformational change in the eukaryotic
1343 translation preinitiation complex and release of eIF1 signal recognition of the start codon. *Mol. Cell* 17, 265-275
1344 [10.1016/j.molcel.2004.11](https://doi.org/10.1016/j.molcel.2004.11).

1345

1346 Malygin, A.A., Kossinova, O.A., Shatsky, I.N., and Karpova, G.G. (2013a). HCV IRES interacts with the 18S rRNA
1347 to activate the 40S ribosome for subsequent steps of translation initiation. *Nucleic Acids Res.* 41, 8706-8714.
1348 [10.1093/nar/gkt632](https://doi.org/10.1093/nar/gkt632).

1349

1350 Malygin, A.A., Shatsky, I.N., and Karpova, G.G. (2013b). Proteins of the human 40S ribosomal subunit involved in
1351 hepatitis C IRES binding as revealed from fluorescent labeling. *Biochemistry (Mosc).* 78, 53-59.
1352 [10.1134/S0006297913010069](https://doi.org/10.1134/S0006297913010069).

1353

1354 Marintchev, A., Kolupaeva, V.G., Pestova, T.V., and Wagner, G. (2003). Mapping the binding interface between
1355 human eukaryotic initiation factors 1A and 5B: a new interaction between old partners. Proc. Natl. Acad. Sci. U.S.A.
1356 100, 1535-1440. [10.1073/pnas.0437845100](https://doi.org/10.1073/pnas.0437845100).

1357

1358 Matsuda, D., and Mauro, V.P. (2014). Base pairing between hepatitis C virus RNA and 18S rRNA is required for
1359 IRES-dependent translation initiation in vivo. Proc. Natl. Acad. Sci. U.S.A. 111, 15385-15389.
1360 [10.1073/pnas.1413472111](https://doi.org/10.1073/pnas.1413472111).

1361

1362 Morin, A., Eisenbraun, B., Key, J., Sanschagrin, P.C., Timony, M.A., Ottaviano, M. and Sliz, P., (2013). Cutting edge:
1363 Collaboration gets the most out of software. Elife. 2, e01456. [10.7554/eLife.01456](https://doi.org/10.7554/eLife.01456).

1364

1365 Nag, N., Lin, K.Y., Edmonds, K.A., Yu, J., Nadkarni, D., Marintcheva, B., and Marintchev, A. (2016). eIF1A/eIF5B
1366 interaction network and its functions in translation initiation complex assembly and remodeling. Nucleic Acids Res.
1367 44, 7441-7456. [10.1093/nar/gkw552](https://doi.org/10.1093/nar/gkw552).

1368

1369 Neupane R, Pisareva VP, Rodriguez CF, Pisarev AV, Fernández IS. (2020) A complex IRES at the 5'-UTR of a viral
1370 mRNA assembles a functional 48S complex via an uAUG intermediate. Elife. 9, e54575. [10.7554/eLife.54575](https://doi.org/10.7554/eLife.54575).

1371

1372 Odreman-Macchioli, F., Baralle, F.E., and Buratti, E. (2001). Mutational analysis of the different bulge regions of
1373 hepatitis C virus domain II and their influence on internal ribosome entry site translational ability. J Biol Chem. 276,
1374 41648-41655. [10.1074/jbc.M104128200](https://doi.org/10.1074/jbc.M104128200).

1375

1376 Passmore, L.A., and Russo, C.J. (2016). Specimen Preparation for High-Resolution Cryo-EM. Methods Enzymol.
1377 579, 51-86. [10.1016/bs.mie.2016.04.011](https://doi.org/10.1016/bs.mie.2016.04.011).

1378

1379 Passmore, L.A., Schmeing, T.M., Maag, D., Applefield, D.J., Acker, M.G., Algire, M.A., Lorsch, J.R., and
1380 Ramakrishnan, V. (2007). The eukaryotic translation initiation factors eIF1 and eIF1A induce an open conformation
1381 of the 40S ribosome. Mol. Cell 26, 41-50. [10.1016/j.molcel.2007.03.018](https://doi.org/10.1016/j.molcel.2007.03.018).

1382

1383 Pestova, T.V., and Hellen, C.U. (2001). Preparation and activity of synthetic unmodified mammalian tRNAi(Met) in
1384 initiation of translation in vitro. RNA 7, 1496-1505. [10.1017/s135583820101038x](https://doi.org/10.1017/s135583820101038x).

1385

1386 Pestova, T.V., and Kolupaeva, V.G. (2002). The roles of individual eukaryotic translation initiation factors in
1387 ribosomal scanning and initiation codon selection. Genes Dev. 16, 2906-2922. [10.1101/gad.1020902](https://doi.org/10.1101/gad.1020902).

1388

1389 Pestova, T.V., Borukhov, S.I., and Hellen, C.U. (1998a). Eukaryotic ribosomes require initiation factors 1 and 1A to
1390 locate initiation codons. Nature 394, 854-859. [10.1038/29703](https://doi.org/10.1038/29703).

1391
1392 Pestova, T.V., Shatsky, I.N., Fletcher, S.P., Jackson, R.J., and Hellen, C.U. (1998b). A prokaryotic-like mode of
1393 cytoplasmic eukaryotic ribosome binding to the initiation codon during internal translation initiation of hepatitis C
1394 and classical swine fever virus RNAs. *Genes Dev.* 12, 67-83. [10.1101/gad.12.1.67](https://doi.org/10.1101/gad.12.1.67).
1395
1396 Pestova, T.V., Lomakin, I.B., Lee, J.H., Choi, S.K., Dever, T.E., and Hellen, C.U. (2000). The joining of ribosomal
1397 subunits in eukaryotes requires eIF5B. *Nature* 403, 332-335. [10.1038/35002118](https://doi.org/10.1038/35002118).
1398
1399 Pestova, T.V., de Breyne, S., Pisarev, A.V., Abaeva, I.S., and Hellen, C.U. (2008). eIF2-dependent and eIF2-
1400 independent modes of initiation on the CSFV IRES: a common role of domain II. *EMBO J.* 27, 1060-1072.
1401 [10.1038/emboj.2008.49](https://doi.org/10.1038/emboj.2008.49).
1402
1403 Pettersen, E.F., Goddard, T.D., Huang, C.C., Couch, G.S., Greenblatt, D.M., Meng, E.C., and Ferrin, T.E. (2004).
1404 UCSF Chimera--a visualization system for exploratory research and analysis. *J. Comput. Chem.* 25, 1605-12.
1405 [10.1002/jcc.20084](https://doi.org/10.1002/jcc.20084).
1406
1407 Pisarev, A.V., Kolupaeva, V.G., Pisareva, V.P., Merrick, W.C., Hellen, C.U., and Pestova, T.V. (2006). Specific
1408 functional interactions of nucleotides at key -3 and +4 positions flanking the initiation codon with components of the
1409 mammalian 48S translation initiation complex. *Genes Dev.* 20, 624-36. [10.1101/gad.1397906](https://doi.org/10.1101/gad.1397906)
1410
1411 Pisarev, A.V., Unbehaun, A., Hellen, C.U., and Pestova, T.V. (2007). Assembly and analysis of eukaryotic translation
1412 initiation complexes. *Methods Enzymol.* 430, 147-77. [10.1016/S0076-6879\(07\)30007-4](https://doi.org/10.1016/S0076-6879(07)30007-4).
1413
1414 Pisareva, V.P., Pisarev, A.V., and Fernández, I.S. (2018). Dual tRNA mimicry in the cricket paralysis virus IRES
1415 uncovers an unexpected similarity with the hepatitis C virus IRES. *Elife* 7, e34062. [10.7554/elife.34062](https://doi.org/10.7554/elife.34062).
1416
1417 Potter, C.S., Chu, H., Frey, B., Green, C., Kisseberth, N., Madden, T.J., Miller, K.L., Nahrstedt, K., Pulokas, J.,
1418 Reilein, A., Tcheng, D., Weber, D., and Carragher, B. (1999). Leginon: a system for fully automated acquisition of
1419 1000 electron micrographs a day. *Ultramicroscopy* 77, 153-161. [10.1016/s0304-3991\(99\)00043-1](https://doi.org/10.1016/s0304-3991(99)00043-1).
1420
1421 Prince, J.B., Taylor, B.H., Rhurlow, D.L., Ofengand, J., and Zimmermann, R.A. (1982). Covalent crosslinking of
1422 tRNA₁^{Val} to 16S RNA at the ribosomal P site: identification of crosslinked residues. *Proc. Natl. Acad. Sci. U.S.A.* 79,
1423 5450-5454. [10.1073/pnas.79.18.5450](https://doi.org/10.1073/pnas.79.18.5450).
1424
1425 Quade, N., Boehringer, D., Leibundgut, M., van den Heuvel, J., and Ban, N. (2015). Cryo-EM structure of Hepatitis
1426 C virus IRES bound to the human ribosome at 3.9-Å resolution. *Nat. Commun.* 6, 7646. [10.1038/ncomms8646](https://doi.org/10.1038/ncomms8646).
1427

1428 Reibarkh, M., Yamamoto, Y., Singh, C.R., del Rio, F., Fahmy, A., Lee, B., Luna, R.E., Ii, M., Wagner, G., and Asano, K. (2008). Eukaryotic initiation factor (eIF) 1 carries two distinct eIF5-binding faces important for multifactor assembly and AUG selection. *J. Biol. Chem.* 283, 1094-1103. [10.1074/jbc.M708155200](https://doi.org/10.1074/jbc.M708155200).

1429

1430

1431

1432 Reynolds, J.E., Kaminski, A., Carroll, A.R., Clarke, B.E., Rowlands, D.J., and Jackson, R.J. (1996). Internal initiation of translation of hepatitis C virus RNA: the ribosome entry site is at the authentic initiation codon. *RNA* 2, 867-878.

1433

1434

1435 Rohou, A., and Grigorieff, N. (2015). CTFFIND4: Fast and accurate defocus estimation from electron micrographs. *J. Struct. Biol.* 192, 216-221. [10.1016/j.jsb.2015.08.008](https://doi.org/10.1016/j.jsb.2015.08.008).

1436

1437

1438 Rosenthal, P.B., and Henderson, R., (2003). Optimal determination of particle orientation, absolute hand, and contrast loss in single-particle electron cryomicroscopy. *J. Mol. Biol.* 333, 721-745. [10.1016/j.jmb.2003.07.013](https://doi.org/10.1016/j.jmb.2003.07.013).

1439

1440

1441 Scheres, S.H. (2012). RELION: implementation of a Bayesian approach to cryo-EM structure determination. *J. Struct. Biol.* 180, 519-530. [10.1016/j.jsb.2012.09.006](https://doi.org/10.1016/j.jsb.2012.09.006).

1442

1443

1444 Scheres, S.H. (2016). Processing of structurally heterogeneous cryo-EM data in RELION. *Methods. Enzymol.* 579, 125-157. [10.1016/bs.mie.2016.04.012](https://doi.org/10.1016/bs.mie.2016.04.012)

1445

1446

1447 Schrödinger, L.L.C. (2015). The PyMOL Molecular Graphics System, Version 2.4.1 (Shrodinger LLC). <https://pymol.org/>

1448

1449

1450 Simonetti, A., Brito Querido, J., Myasnikov, A.G., Mancera-Martinez, E., Renaud, A., Kuhn, L., and Hashem Y. (2016). eIF3 Peripheral Subunits Rearrangement after mRNA Binding and Start-Codon Recognition. *Mol. Cell* 63, 206-217. [10.1016/j.molcel.2016.05.033](https://doi.org/10.1016/j.molcel.2016.05.033).

1451

1452

1453

1454 Simonetti, A., Guca, E., Bochler, A., Kuhn, L., and Hashem, Y. (2020). Structural insights into the mammalian late-stage initiation complexes. *Cell Rep.* 31, 107497. [10.1016/j.celrep.2020.03.061](https://doi.org/10.1016/j.celrep.2020.03.061)

1455

1456

1457 Sizova, D.V., Kolupaeva, V.G., Pestova, T.V., Shatsky, I.N., and Hellen, C.U. (1998). Specific interaction of eukaryotic translation initiation factor 3 with the 5' nontranslated regions of hepatitis C virus and classical swine fever virus RNAs. *J. Virol.* 72, 4775-4782. [10.1128/JVI.72.6.4775-4782.1998](https://doi.org/10.1128/JVI.72.6.4775-4782.1998).

1458

1459

1460

1461 Spahn, C.M., Kieft, J.S., Grassucci, R.A., Penczek, P.A., Zhou, K., Doudna, J.A., and Frank, J. (2001). Hepatitis C virus IRES RNA-induced changes in the conformation of the 40s ribosomal subunit. *Science* 291, 1959-1962. [10.1126/science.1058409](https://doi.org/10.1126/science.1058409).

1462

1463

1464

1465 Suloway, C., Pulokas, J., Fellmann, D., Cheng, A., Guerra, F., Quispe, J., Stagg, S., Potter, C.S., and Carragher, B.
1466 (2005). Automated molecular microscopy: the new Leginon system. *J. Struct. Biol.* 151, 41-60.
1467 10.1016/j.jsb.2005.03.010.

1468

1469 Tang, S., Collier, A.J., and Elliott, R.M. (1999). Alterations to both primary and predicted secondary structure of stem-
1470 loop IIIc of the hepatitis C virus 1b 5' untranslated region 5'UTR) lead to mutants severely defective in translation
1471 which cannot be complemented in trans by the wild-type 5'UTR sequence. *J. Virol.* 73, 2359-2364.
1472 10.1128/JVI.73.3.2359-2364.1999.

1473

1474 Terenin, I.M., Dmitriev, S.E., Andreev, D.E., and Shatsky, I.N. (2008). Eukaryotic translation initiation machinery
1475 can operate in a bacterial-like mode without eIF2. *Nat. Struct. Mol. Biol.* 15, 836-841. 10.1038/nsmb.1445.

1476

1477 Thakur, A., Gaikwad, S., Vijamarri, A.K., and Hinnebusch, A.G. (2020). eIF2 α interactions with mRNA control
1478 accurate start codon selection by the translation preinitiation complex. *Nucleic Acids Res.* 48, 810280-10296.
1479 10.1093/nar/gkaa761.

1480

1481 Tivol, W.F., Briegel, A., and Jensen, G.J. (2008). An improved cryogen for plunge freezing. *Microsc. Microanal.* 14,
1482 375-379. 10.1017/S1431927608080781.

1483

1484 Unbehaun, A., Borukhov, S.I., Hellen, C.U., and Pestova, T.V. (2004). Release of initiation factors from 48S
1485 complexes during ribosomal subunit joining and the link between establishment of codon-anticodon base-pairing and
1486 hydrolysis of eIF2-bound GTP. *Genes Dev.* 18, 3078-3093. 10.1101/gad.1255704.

1487

1488 Wang, J., Wang, J., Shin, B.S., Kim, J.R., Dever, T.E., Puglisi, J.D., and Fernández, I.S. (2020). Structural basis for
1489 the transition from translation initiation to elongation by an 80S-eIF5B complex. *Nat. Commun.* 11, 5003.
1490 10.1038/s41467-020-18829-3.

1491

1492 Yamamoto, H., Unbehaun, A., Loerke, J., Behrmann, E., Collier, M., Bürger, J., Mielke, T., and Spahn, C.M. (2014).
1493 Structure of the mammalian 80S initiation complex with initiation factor 5B on HCV-IRES RNA. *Nat. Struct. Mol.*
1494 *Biol.* 21, 721-727. 10.1038/nsmb.2859.

1495

1496 Yamamoto, H., Collier, M., Loerke, J., Ismer, J., Schmidt, A., Hilal, T., Sprink, T., Yamamoto, K., Mielke, T., Bürger,
1497 J., Shaikh, T.R., Dabrowski, M., Hildebrand, P.W., Scheerer, P., and Spahn, C.M. (2015). Molecular architecture of
1498 the ribosome-bound Hepatitis C Virus internal ribosomal entry site RNA. *EMBO J.* 34, 3042-3058.
1499 10.15252/embj.201592469.

1500

1501 Yokoyama, T., Machida, K., Iwasaki, W., Shigeta, T., Nishimoto, M., Takahashi, M., Sakamoto, A., Yonemochi, M.,
1502 Harada, Y., Shigematsu, H., Shirouzu, M., Tadakuma, H., Imataka, H., and Ito, T. (2019). HCV IRES captures an
1503 actively translating 80S ribosome. *Mol. Cell* 74, 1205-1214.e8. [10.1016/j.molcel.2019.04.022](https://doi.org/10.1016/j.molcel.2019.04.022).

1504

1505 Zheng, A., Yu, J., Yamamoto, R., Ose, T., Tanaka, I., and Yao, M. (2014). X-ray structures of eIF5B and the eIF5B-
1506 eIF1A complex: the conformational flexibility of eIF5B is restricted on the ribosome by interaction with eIF1A. *Acta
1507 Crystallogr. D Biol. Crystallogr.* 70, 3090-3098. [10.1107/S1399004714021476](https://doi.org/10.1107/S1399004714021476).

1508

1509 Zheng, S.Q., Palovcak, E., Armache, J.P., Verba, K.A., Cheng, Y., and Agard, D.A. (2017). MotionCor2: anisotropic
1510 correction of beam-induced motion for improved cryo-electron microscopy. *Nat. Methods* 14, 331-332.
1511 [10.1038/nmeth.4193](https://doi.org/10.1038/nmeth.4193).

1512

1513 Zivanov, J., Nakane, T., Forsberg, B.O., Kimanius, D., Hagen, W.J., Lindahl, E. and Scheres, S.H.W. (2018). New
1514 tools for automated high-resolution cryo-EM structure determination in RELION-3. *Elife* 7, e42166.
1515 [10.7554/eLife.42166](https://doi.org/10.7554/eLife.42166)

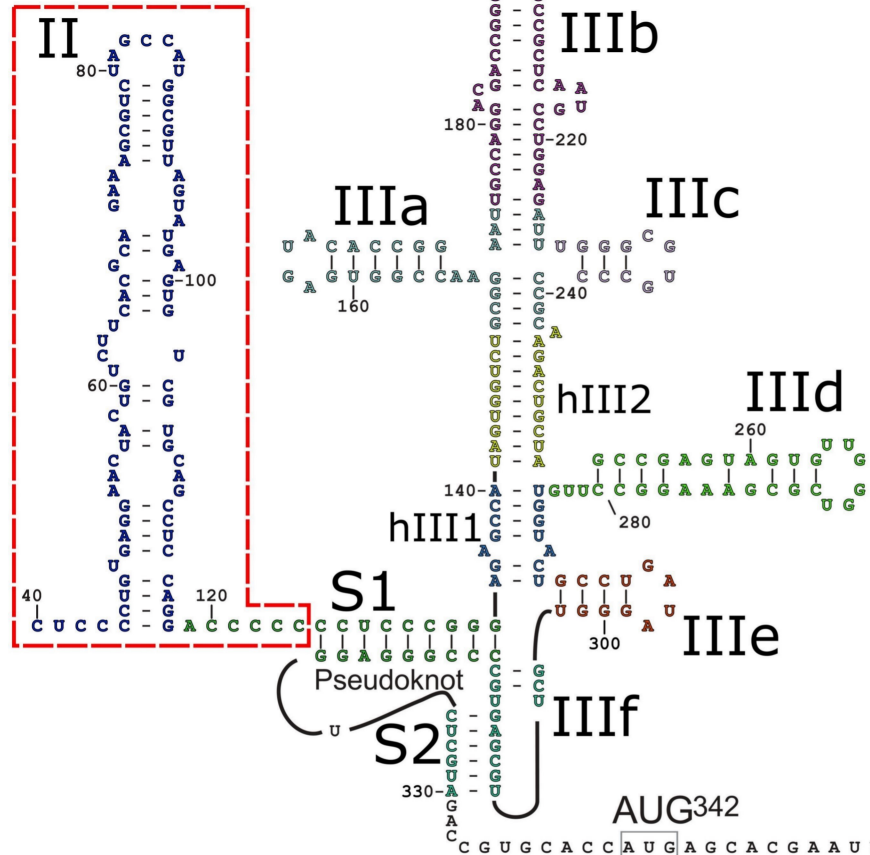
1516

1517 Zivanov, J., Nakane, T., and Scheres, S.H.W. (2019). A Bayesian approach to beam-induced motion correction in
1518 cryo-EM single-particle analysis. *IUCr. J.* 6, 5-17. [10.1107/S205225251801463X](https://doi.org/10.1107/S205225251801463X)

1519

A

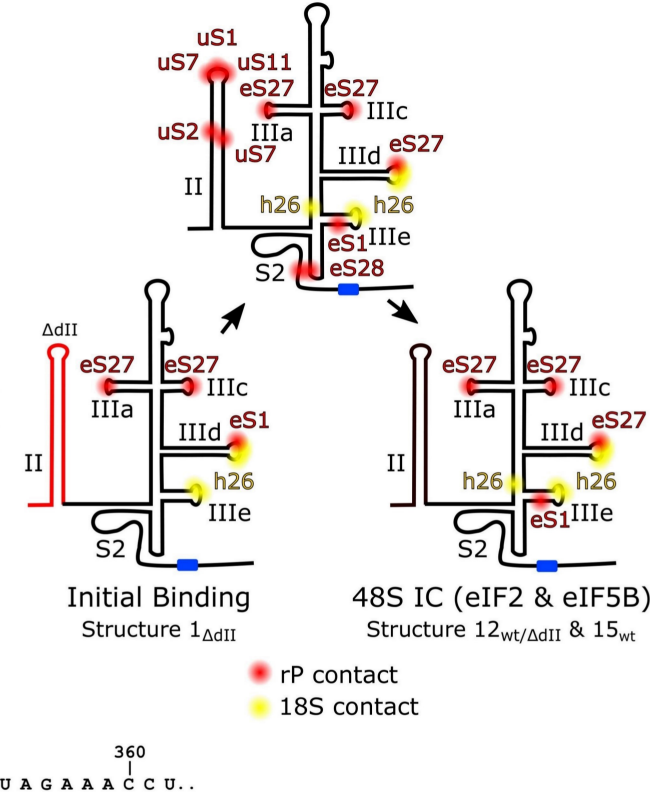
Removed for Δ dII



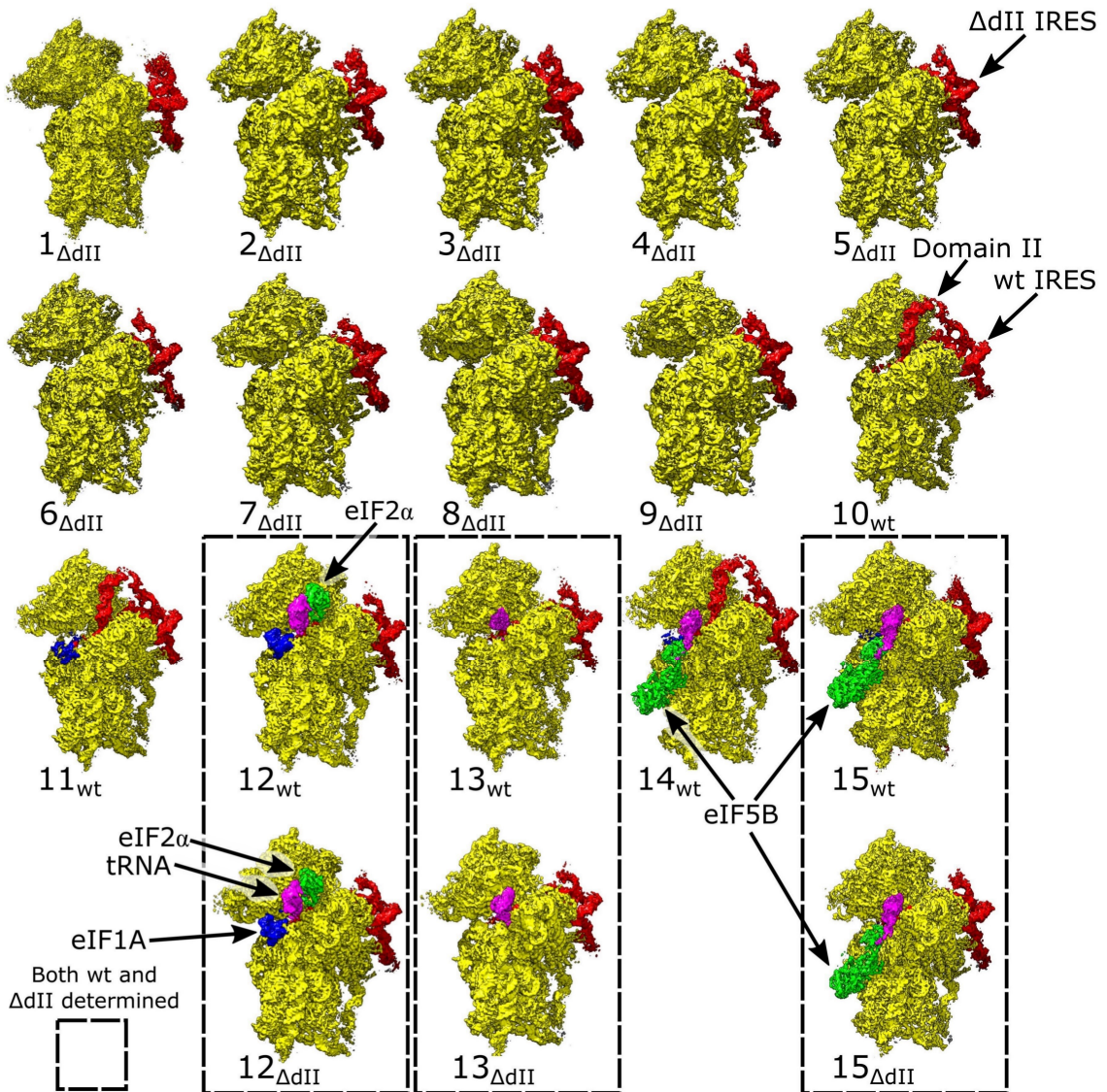
Brown et al. Figure 1

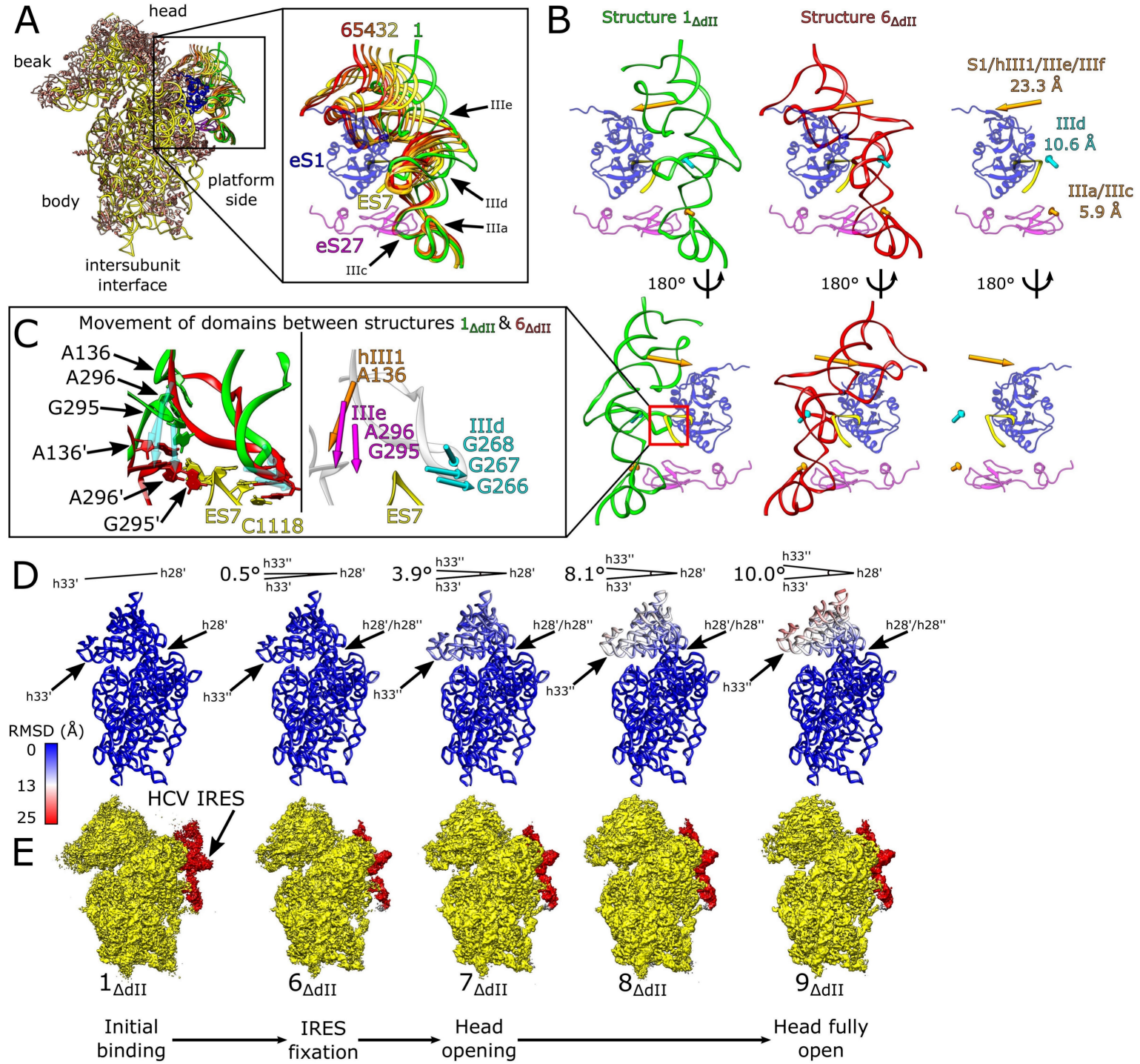
Ternary complex & Pre-48S IC (eIF5B)

Structure 11_{wt} & 14_{wt}

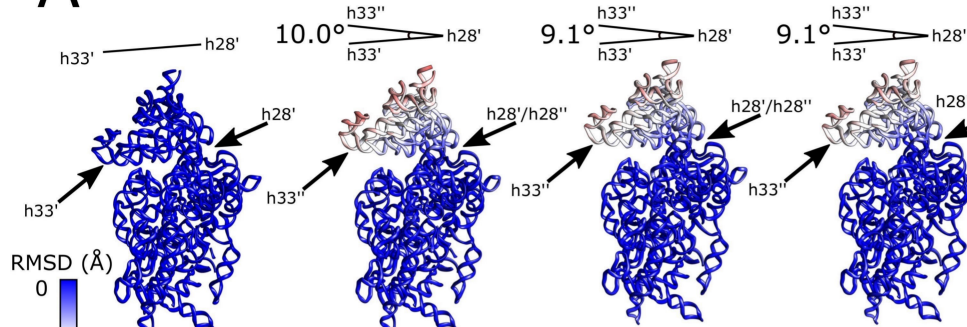


B

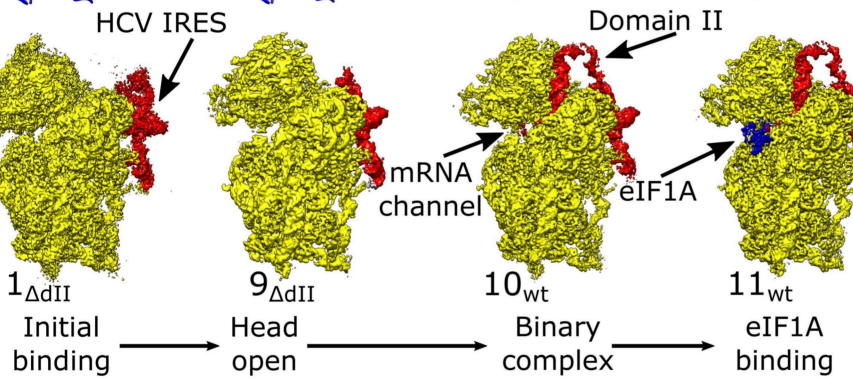




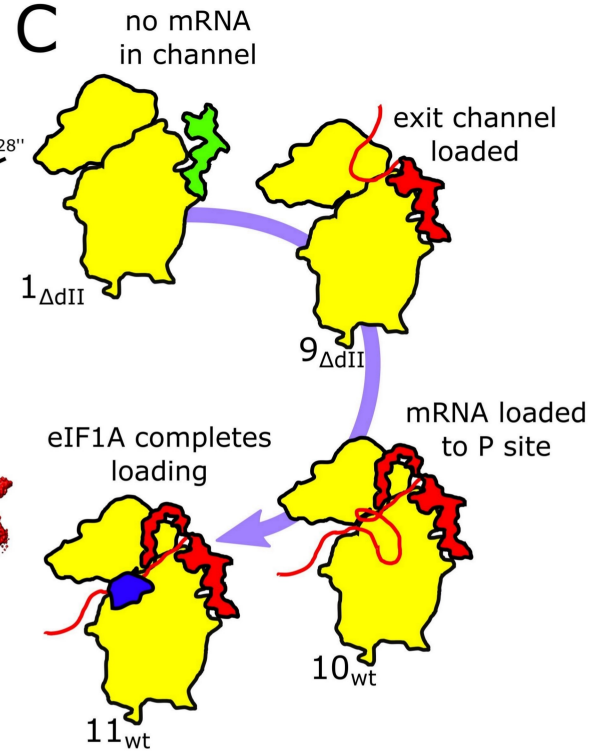
A



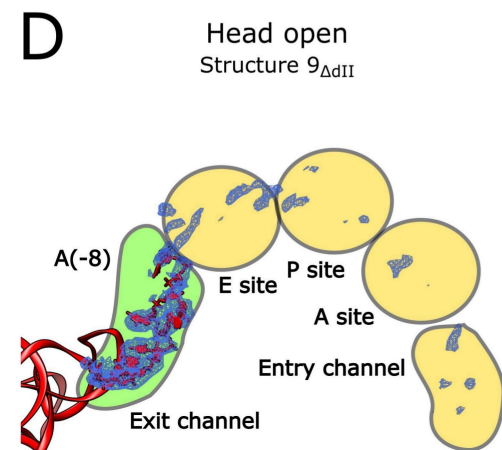
B



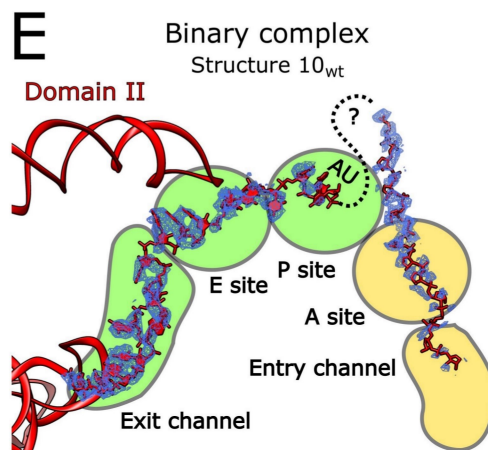
C



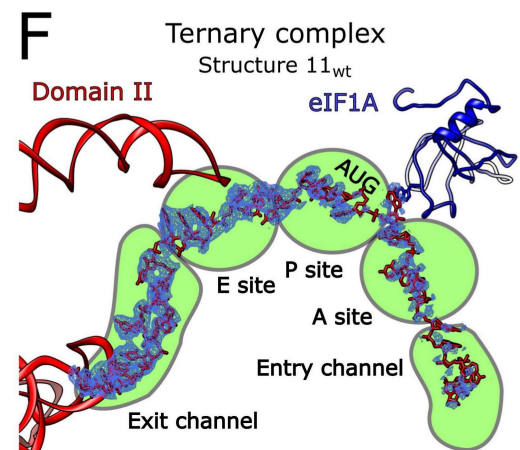
D



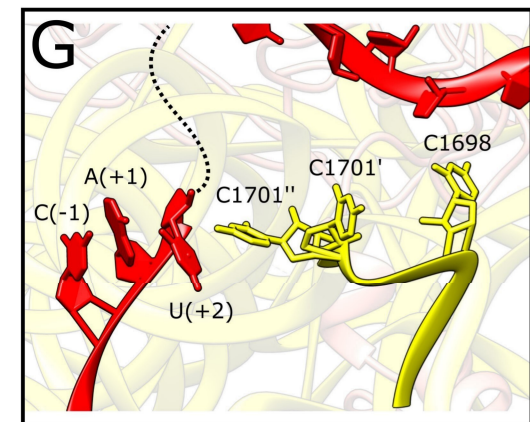
E



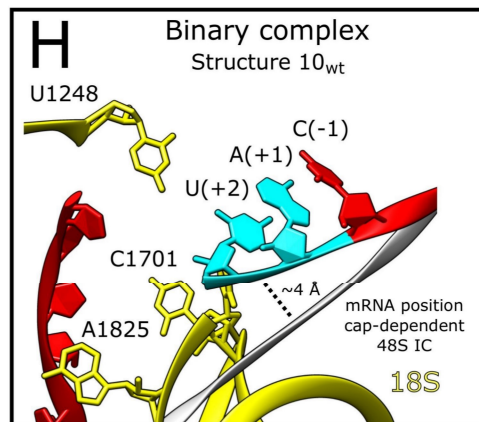
F



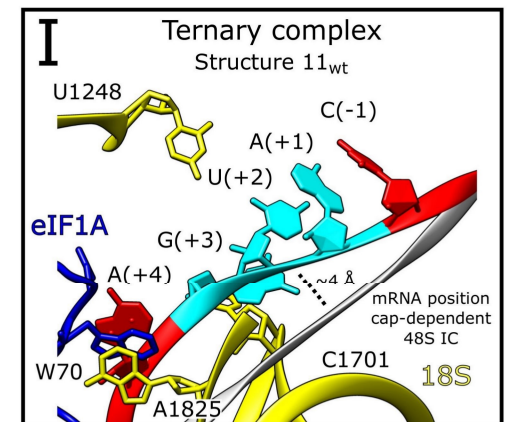
G



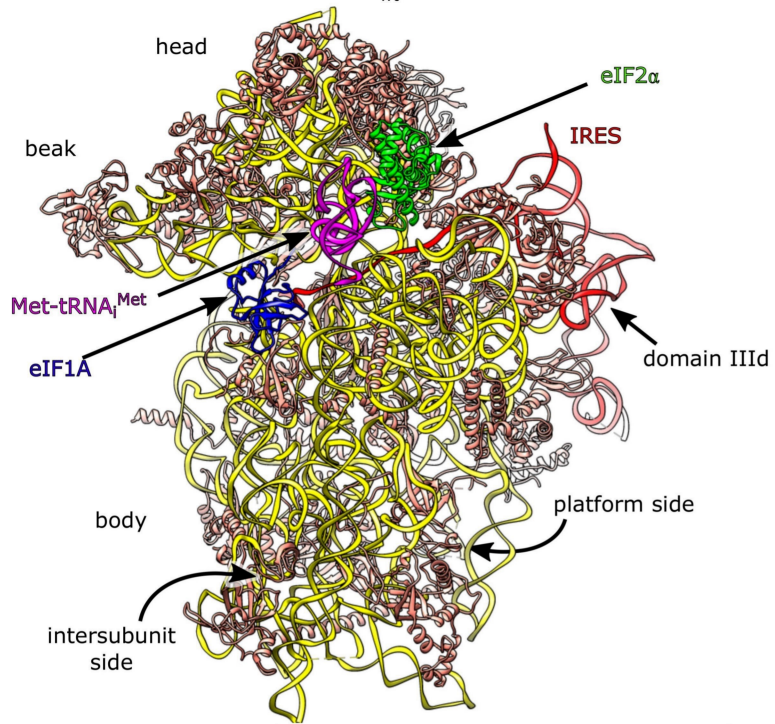
H



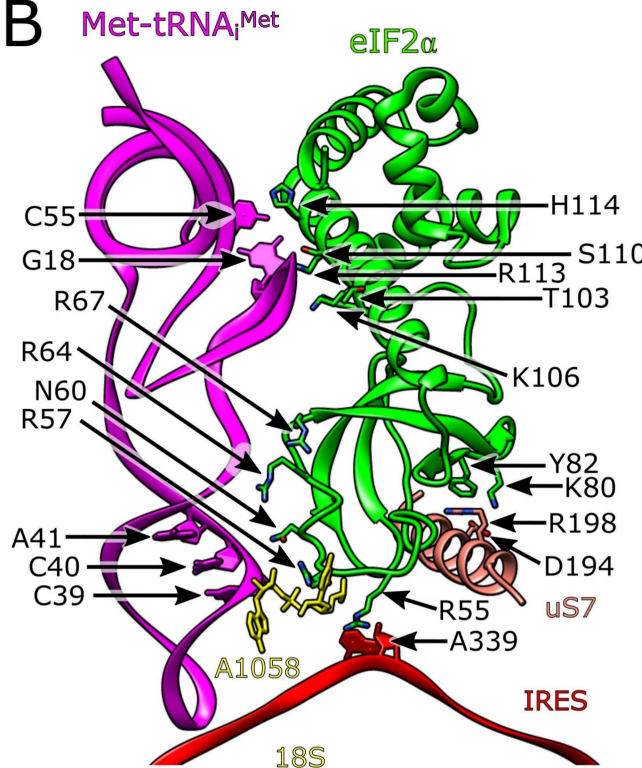
I



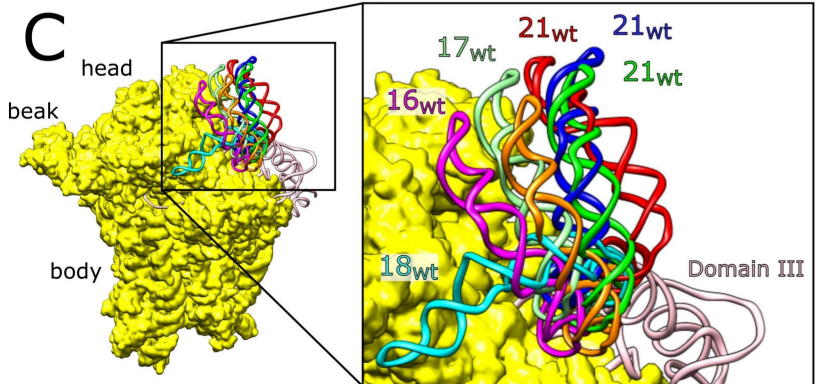
A



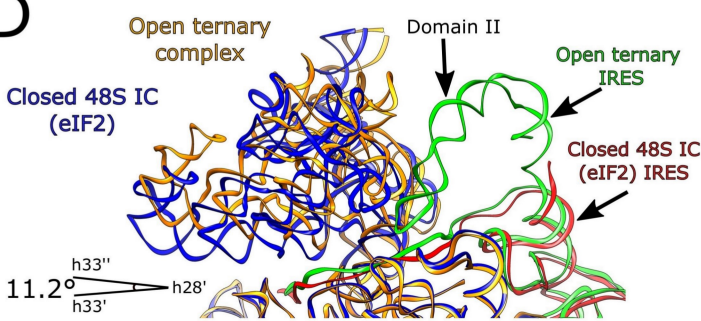
B



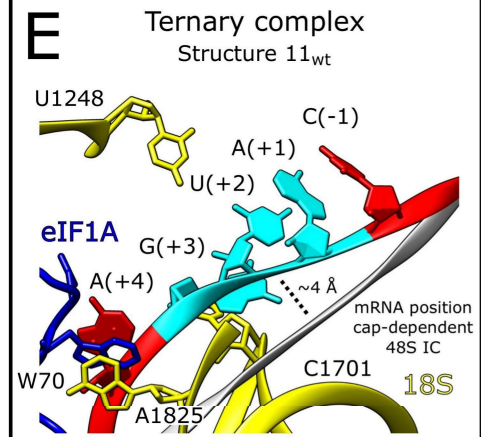
C



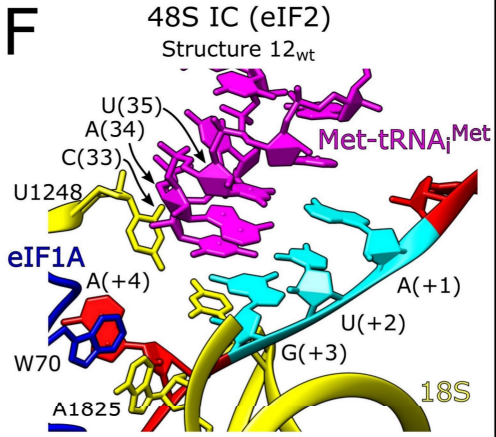
D



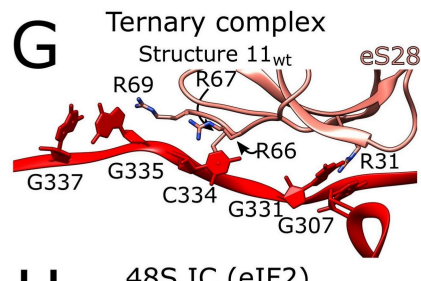
E



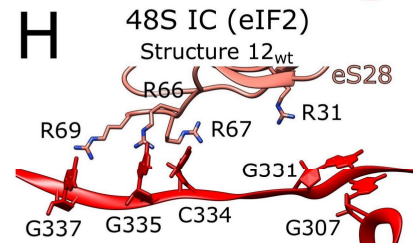
F



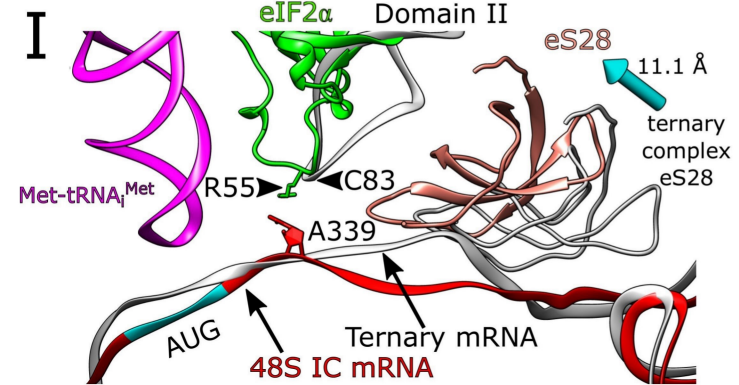
G



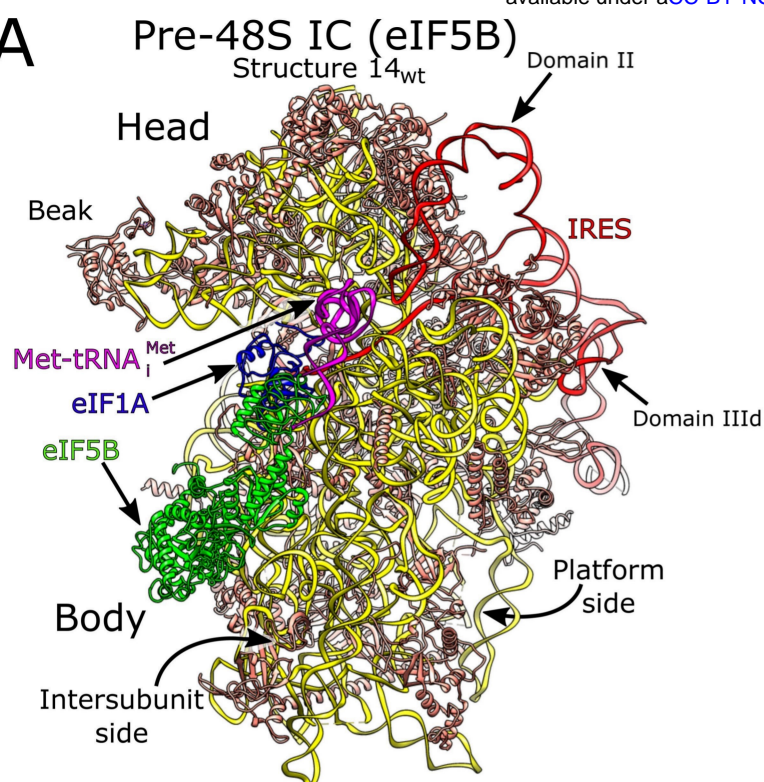
H



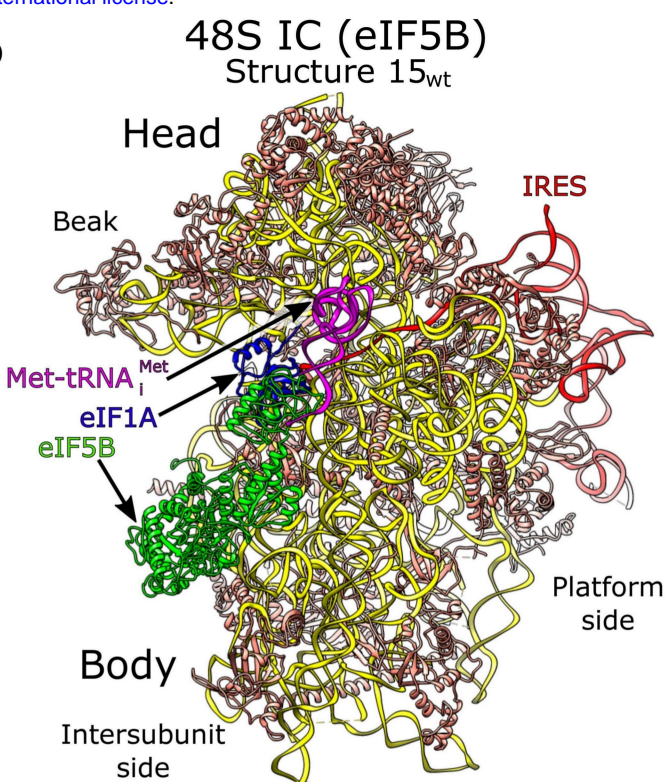
I



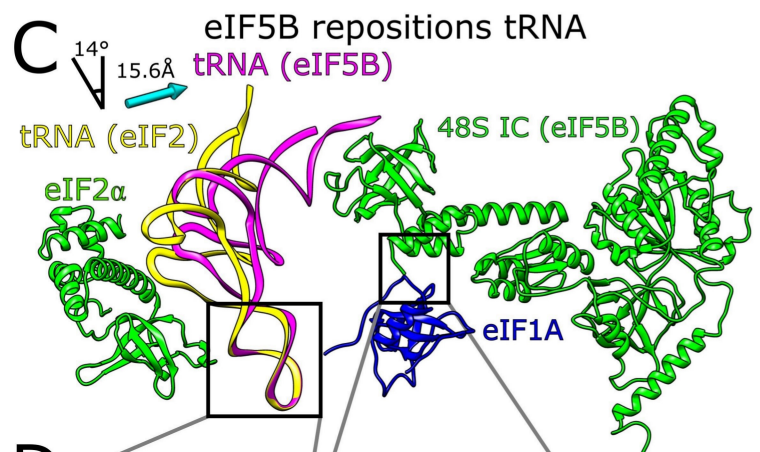
A



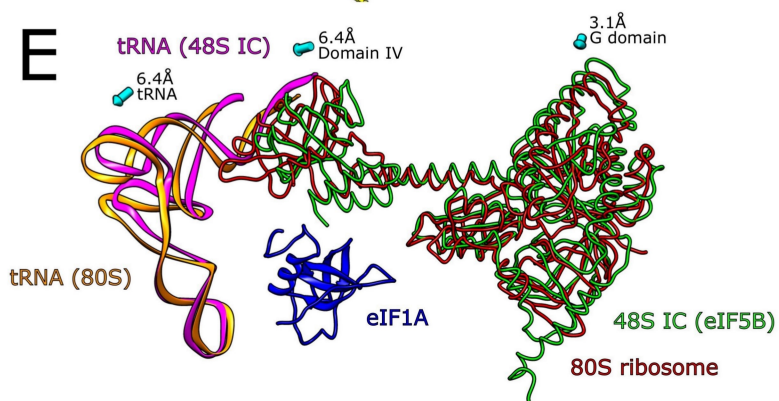
B



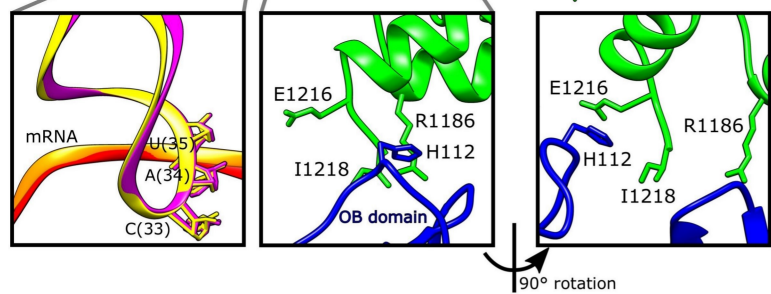
C



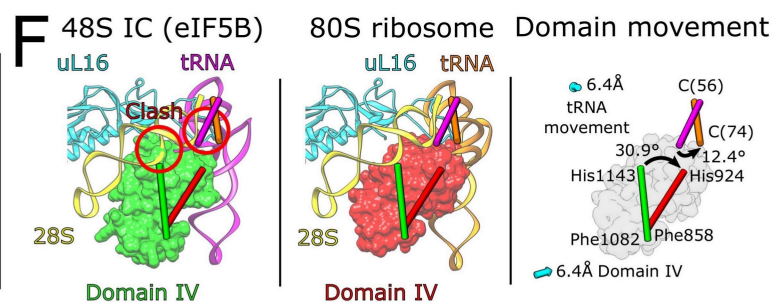
E



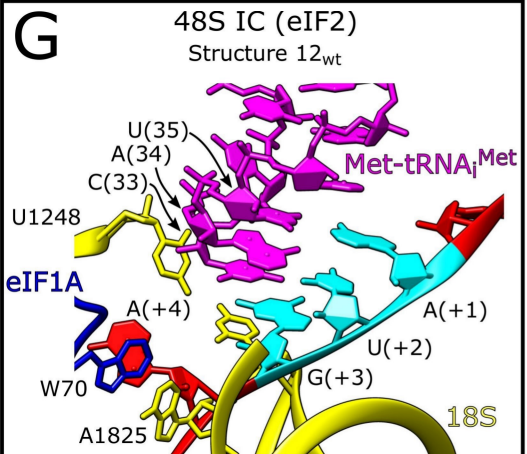
D



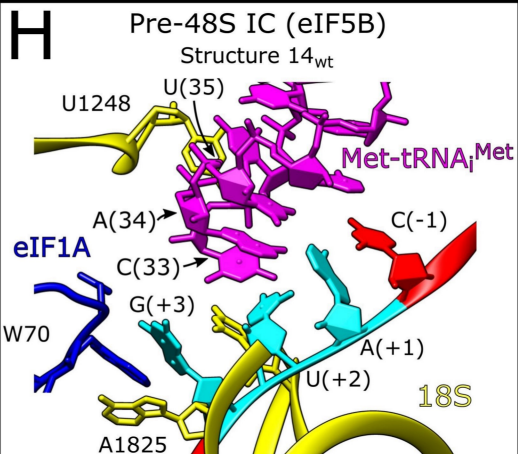
F



G



H



I

